Univerzita Karlova v Praze
Matematicko-fyzikální fakulta

DIPLOMOVÁ PRÁCE

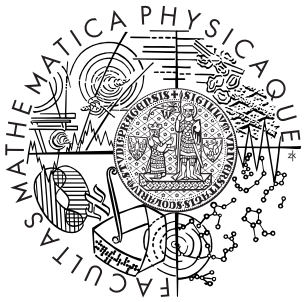

Boris Bulánek

Analýza dat kalorimetru CALICE

Ústav částicové a jaderné fyziky

Vedoucí diplomové práce: prof. Ing. Josef Žáček, DrSc.
Studijní program: Fyzika, jaderná a subjaderná fyzika.

2010

Acknowledgment

I would like to address special thanks to Josef Žáček supervisor of my diploma thesis for his stimulating interest during the preparation of this thesis and for the possibility of my participation at the FLC group in DESY.

I want to thank many members of people from the FLC group in DESY. I need specially to mention Erika Garutti and Andrea Vargas whose encouragement and support were very valuable for me.

Finally, I would like to thank my family for the steady support I felt during all my study at Charles University and especially in the time of making this thesis.

Prohlašuji, že jsem svou diplomovou práci napsal samostatně a výhradně s použitím citovaných pramenů. Souhlasím se zapůjčováním práce.

V Praze dne 20. dubna 2010 Boris Bulánek

Contents

Název práce: Analýza dat kalorimetru CALICE
Autor: Boris Bulánek
Katedra (ústav): Ústav částicové a jaderné fyziky
Vedoucí diplomové práce: prof. Ing. Josef Žáček, DrSc.
E-mail vedoucího: zacek@ipnp.troja.mff.cuni.cz

Abstrakt: V predloženej práci študujeme kalibračnú metódu hadrónového kalorimetru. Kalibračný proces je rozdelený do troch častí. V prvej časti je popísaný princíp kalibrácie. Zároveň sú porovnávané výsledky s predchodzími výsledkami. Metóda teplotnej a napäťovej korekcie je popísaná v druhej časti. Taktiež sú porovnané výsledky s už obdržanými výsledkami. Posledná časť je venovaná popisu hľadania miónových dráh. Bol vytvorený modifikovaný algoritmus hľadania miónových dráh a porovnávaný s predchádzajúcim algoritmom.

Klíčová slova: kalorimeter, kalibrácia, lineárny urýchlovač

Title: Data analysis of the calorimeter CALICE
Author: Boris Bulánek
Department: Institute of Particle and Nuclear Physics
Supervisor: prof. Ing. Josef Žáček, DrSc.
Supervisor's e-mail address: zacek@ipnp.troja.mff.cuni.cz

Abstract: In the present work we study the muon calibration of a hadronic calorimeter. The calibration issue is divided into three parts. Description of the calibration principle and a comparison of the results with the previous results is described in the first part. The method of the temperature and voltage corrections is presented in the second part. Also a comparison between the new and previous results is included. The last part is devoted to the study of muon track finding. The modified algorithm for searching muons was developed and compared with the default trakfinding algorithm.

Keywords: calorimeter, calibration, linear collider

Chapter 1

Introduction

One of the successes of the high energy physics in the last century was the development of the Standard Model which has explained many effects observed in particle experiments. On the other hand this model has too many parameters and therefore it is believed that there is a new physics beyond the Standard Model. It is expected that experiments at the Large Hadron Collider at CERN will discover the remaining piece of the Standard Model, the Higgs boson or that they will have capabilities to discover new phenomena.

To improve the accuracy of the LHC discoveries the worldwide particle physics community has proposed the construction of the International Linear Collider (ILC) where beams of electrons and positrons will collide. This collider will become the main device for particle physics in the after-LHC period. The collider and detector concepts have been summarized in the Reference Design Report published in 2007. To reach expected detector performance, calorimeter systems with high precision have been proposed with the goal to reconstruct particles and jets in hadronic calorimeters by the method called particle flow. This method requires unprecedented granularity of calorimetres to have a possibility to distinguish particle tracks in hadronic showers.

The collaboration CALICE is a group of institutions from 17 countries working together to develop high performance electromagnetic and hadronic calorimeters. Prague group has been participated in the prototype construction of both devices since 2001. One of the technical solutions of the hadronic calorimeter is the scintillator analog hadronic calorimeter which uses as photodetectors recently developed Silicon Photomultiplierss (SiPM). A physical prototype of the calorimeter has been assembled at DESY and tested with various beams at CERN[1] and FNAL[2].

To reach expected physics features of this prototype a precise calibration method is necessary. In this thesis I present the muon calibration method which

[1] Conseil Eropéenne pour la Recherche Nucléaire

[2] Fermi National Accelerator Laboratory (Fermilab)

I have developed and which is a modification of the method previously applied in the calorimeter data analysis. The results were obtain during my visit in DESY, where I joined the group FLC[3].

After a brief introduction to the ILC, the hadronic calorimeter is described in chapter 4. The principle of the calibration is presented in chapter 6. The method which enables to estimate the temperature and voltage dependence of deposited energy is explained in chapter 7. The modification of the track finding algorithm for the muons is presented in chapter 8.

[3]Forschung mit Lepton Collidern (Research with Lepton Colliders)

Chapter 2

International Linear Collider (ILC)

The ILC is large international project the goal of which is to improve precision of measurements already done at LEP, SLC and Tevatron. Searching for Higgs boson to complete particle gallery of Standard Model is the aim of *Linear Hadronic Collider (LHC)* at CERN.
At ILC the beam of positrons and electrons will be collided. The advantage of a linear collider is the possibility to forget about the problem of synchrotron radiation which is proportional to E^4/m_0^4, where E is the energy of particle and m_0 is the rest mass of particle. Due to m_0 in denominator, it is not possible to use light leptons for high energy collisions in circular accelerators. The advantage of lepton-lepton interaction is a purity of interactions and better knowledge of the initial condition in comparison of hadronic collider. Only with a few modifications, it should be possible to use e^-e^- interactions for measuring of selectron mass or γe and $\gamma\gamma$ interactions. The basic parameter of the ILC, the central mass system (cms) energy $\sqrt{s}$ have to reach $\sqrt{s} = 500$ GeV. It has to be possible to go with cms up to 1 TeV. The cms energy of LHC is for comparison 14 TeV. The total luminosity of the ILC have to reach the value of 500 fb^{-1}. The luminosity of 1000 fb^{-1} should be collected during the operation setup at 500 GeV. The tunnel for ILC should be 31 km long. The ILC complex's schematic picture is shown in Figure 2.1.

The main physical fields where could the ILC improve our knowledge are:

- Higgs physics
- gauge boson coupling coefficients
- top quark physics
- supersymmetry and other alternative scenarios

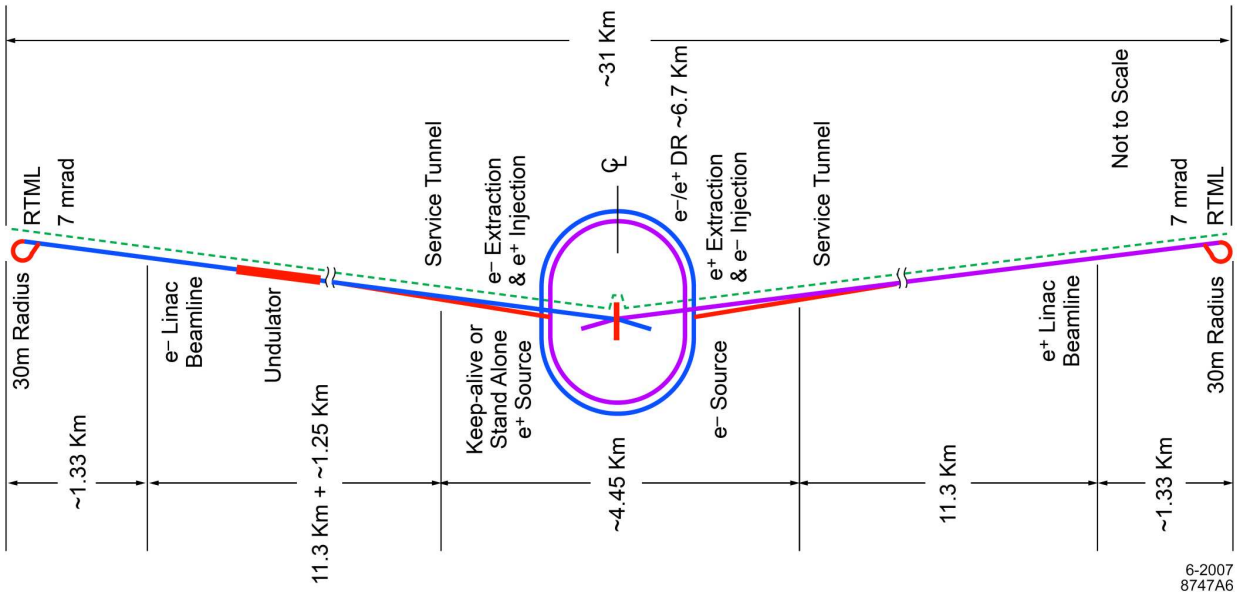

Figure 2.1: Schematic basic plan of the ILC complex. [4]

2.1 Higgs physics

Many analyses devoted to the Higgs physics have been performed with full simulation of detector. The cms energy is adjusted to $\sqrt{s} = 250$ GeV and 500 GeV with luminosity of 250 and 500 fb^{-1}.
The mass of the Higgs boson was assumed to be $m_H = 120$ GeV. The production of the Higgs boson is e.g. in the process $e^+e^- \to ZH$. From the subsequent decay, which is $ZH \to e^+e^-X$ or $ZH \to \mu^+\mu^-X$ the recoil mass m_{recoil} can be determined (X are Higgs decay products). The distributions of the recoil mass for the decay $Z \to e^+e^-$ and $Z \to \mu^+\mu^-$ are shown in the Figure 2.2 [2]. The purity of muon decay channel of Z decay in comparison with the electron decay channel is evident. Larger uncertainty of the energy measurement is effected by the brehmstrahlung and larger background is effected by Bhabha scattering($e^+e^- \to e^+e^-$). The uncertainty of the energy measurement for muon decay channel is basically caused by an uncertainty of momentum measurement.
The uncertainty of m_H is in the best measurement 70 MeV. The precision of m_H is in the case of $Z \to e^+e^-$ worse by factor two in comparison with $Z \to \mu^+\mu^-$.

The study of branching fractions can be regarded as the main program of the ILC. The prove of Higgs boson existence via the Higgs mass determination is the near future task of the LHC. The main reason for Higgs branching fractions study is the possibility to observe the dependence of a Higgs coupling constant on the mass of Higgs boson.

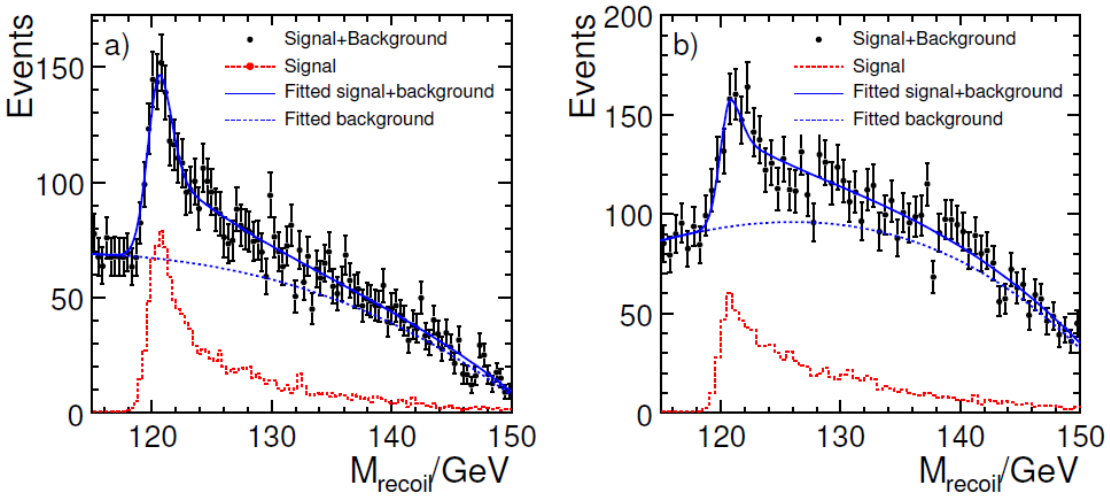

Figure 2.2: Distribution of the recoil mass for the decay $Z \to \mu^+\mu^-$ (left) and $Z \to e^+e^-$ (right).

Chapter 3

International Large Detector (ILD)

The ILD is one of the concepts described in the Reference Design Report [1]. The main processes are decays of intermediate bosons: $Z \rightarrow q\bar{q}$ and $W \rightarrow q\bar{q}$. The precision of di-jet mass detection σ_{m_q}/m_q has to be comparable to $\Gamma_Z/m_Z \approx \Gamma_W/m_W \approx 3-4\%$. The jet energy resolution is requested to be $\sigma_E/E \approx 30\%/\sqrt{E(GeV)}$ what is the needed precision for jets of energies around 100 GeV.

The ILD concept is only one of three still existed detector concepts: Silicon Detector (SiD), 4th concept and ILD. There existed also Global Large Detector concept which was merged with ILD.

The components of ILD going from the interaction point are:

- *Multi-layer vertex detector* with an aim of high point resolution and minimal material thickness.

- *Strip and pixel detectors* to bridge the gap between the vertex detector and time-projection chamber and to measure low angle tracks. They are also between *Time Projection Chamber* and *Electromagnetic Calorimeter*.

- *Time Projection Chamber* for 3-dimensional track resolution with possibility to provide also $\mathrm{d}E/\mathrm{d}x$ particle identification.

- *Electromagnetic Calorimeter (ECAL)* with Si-W or scintilator-tungsten sampling technology. The transverse cell size is 1 x 1 cm^2 what is in the same order as the Moliére radius of tungsten.

- *Hadronic Calorimeter (HCAL)* with highly scintilator tiles of tile size 3×3 cm^2.
  Due to the *particle flow* method to calorimetry, the segmentation is the main characteristics, which is needed to be as fine as it can be. For this reason, there is also propose to construct HCAL with the cell size of 1 x 1 cm^2. The only possibility to construct a calorimeter with such a fine

granularity is to use gas chambers with fine copper pad readout. The signal is then only binary information about deposited energy under or above the threshold value. So we can distinguish two types of hadronic calorimeters for ILD: *Analog hadronic calorimeter (AHCAL)* and the *Digital hadronic calorimeter (DHCAL)*.

- Other detectors to cover almost full 4π angle to measure luminosity and monitor the quality of beam.
- *Superconducting coil* around the whole calorimeter to create an axial magnetic field of 3.5 Tesla.
- *Tail catcher and muon tracker (TCMT)*. The TCMT is a sampling calorimeter. The material of absorber is an iron and scintillator elements are not square cells but 5 x 100 cm strips with a central wavelength shifting fibers. The readout of TCMT is the same as in the case of AHCAL or ECAL.
- Data acquisition (DAQ) without an external trigger.

The whole detector will be mounted on movable platform to use "push-pull" mechanism. All detector concepts use the *Particle flow algorithm* except the 4th

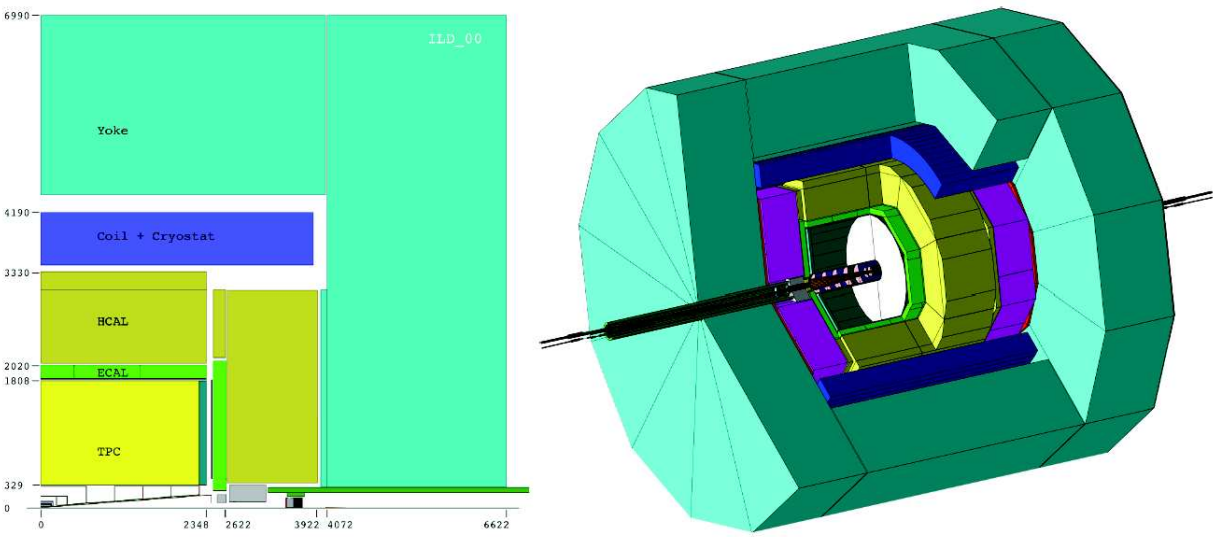

Figure 3.1: Model of ILD with with cut between the beam line on the left side [2].

concept. Therefore it is suitable briefly to describe this algorithm.

3.1 Particle Flow

The main goal of this algorithm is to distinguish separate components of jets and to use for every recognized particle the most convenient part of calorimeter. We can distinguish four basic types of particles of jets with an average percentage after interaction[1]:

- 62 % of charged particles, mainly hadrons
- 27 % of photons
- 10 % neutral, long lived hadrons
- 1.5 % neutrinos

The momentum of charged particles are measured in *TPC*, energy of photons measured in the *ECAL* and of neutral hadrons in the *HCAL*. To distinguish neutral particles and charged particles, it is also necessary to have a possibility to separate particles in calorimeters. Such a separation implies unprecedented segmentation of cells. For an jet energy measurement resolution σ_{jet} we can write

$$\sigma^2_{jet} = \sigma^2_{h^\pm} + \sigma^2_{\gamma} + \sigma^2_{h^0} + \sigma^2_{conf}, \tag{3.1}$$

where $\sigma_{h^\pm}$ refers to the energy measurement resolution of charged particles, σ_γ of photons and σ_{h^0} of neutral hadrons. The confusion term $\sigma_{confusion}$ accounts for mis-identification of a shower (or part of a shower) due either to inefficiency of the algorithm or due to physical limitation (truly overlapping showers). If there would be no confusion in particle identification, the energy resolution would be $\sigma(E)/E \approx 0.2/\sqrt{E(GeV)}$. The algorithm is implemented as a $C++$ code called *PandoraPFA*. It is possible to use it in framework of toolkit *Marlin*[2] More about Particle Flow is presented in [6]. Schematic picture of particle flow approach is shown in Figure 3.2.

[1] informations got from measurement of jets fragmentation on *LEP* ([8] & [9])

[2] About used software, which include also *Marlin* processors, is devoted chapter 5.

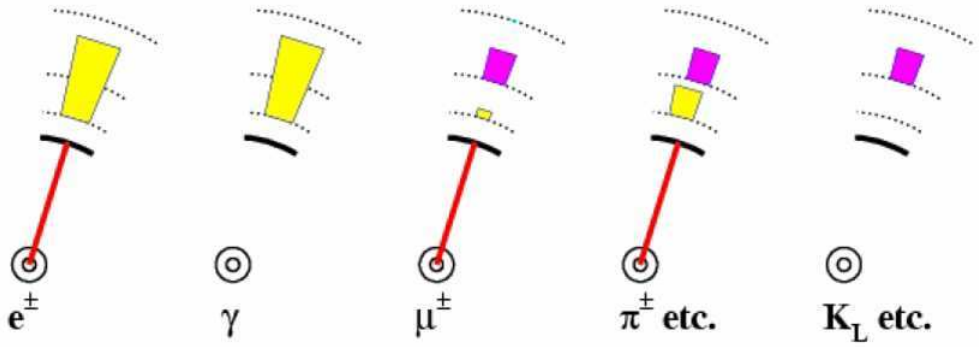

Figure 3.2: Schematic picture of particle separation in the particle flow approach. From left to the right. The momentum of electrons is measured in the tracker, their identification in ECAL. The energy measurement and the identification of photon is performed in ECAL. The muon energy is measured in the tracker and the identification is performed mainly by HCAL and TCMT. The energy of charged hadrons is measured in the tracker and the identification is performed by HCAL. The energy of neutral hadrons is determined in the HCAL. [7]

Chapter 4

CALICE AHCAL

The CALICE (Calorimeter for the Linear Collider Experiment) collaboration was created to coordinate series of R&D activities for detector system for the ILC. The main task of R&D is the verification of the particle flow algorithm. The calorimeter prototypes have been constructed and their performance tested in years 2006 and 2007 at CERN and in 2008 and 2009 at FNAL.

4.1 Description of the AHCAL

The Analog Hadronic Calorimeter (AHCAL) was built with the goal to separate neutral hadrons from charged hadrons, leptons and also photons. Such a detectors should have high granularity both in longitudinal and transversal direction. The AHCAL is built as a sampling calorimeter with a scintillator-steel sandwich structure. The size of one layer is 90×90 cm^2. The number of layers in the AHCAL is 38. The absorber (steel) is 2 cm thick and the active layer (organic scintillator) is 0.5 cm thick. An active layer consists from different square cells. The size of cells are 3×3 cm^2, 6×6 cm^2 and 12×12 cm^2. The cells of size 3×3 cm^2 are only in the inner part of the first 30 layers. The cells of size 6×6 cm^2 are in the outer part of these layers and make the inner part of the last 8 layers. The cells of size 12×12 cm^2 are around all layers. The first 30 layers are called *fine* and the last 8 layers are called *course*. The number of cells is summarized in Table 4.1. The schematic picture of cells in a fine and course layer is shown in

type of layer	# modules	#cells per module	#cells
fine	30	216	6480
course	8	141	1128
course+fine	38	-	7608

Table 4.1: Number of cells in different types of layers.

Figure 4.1.

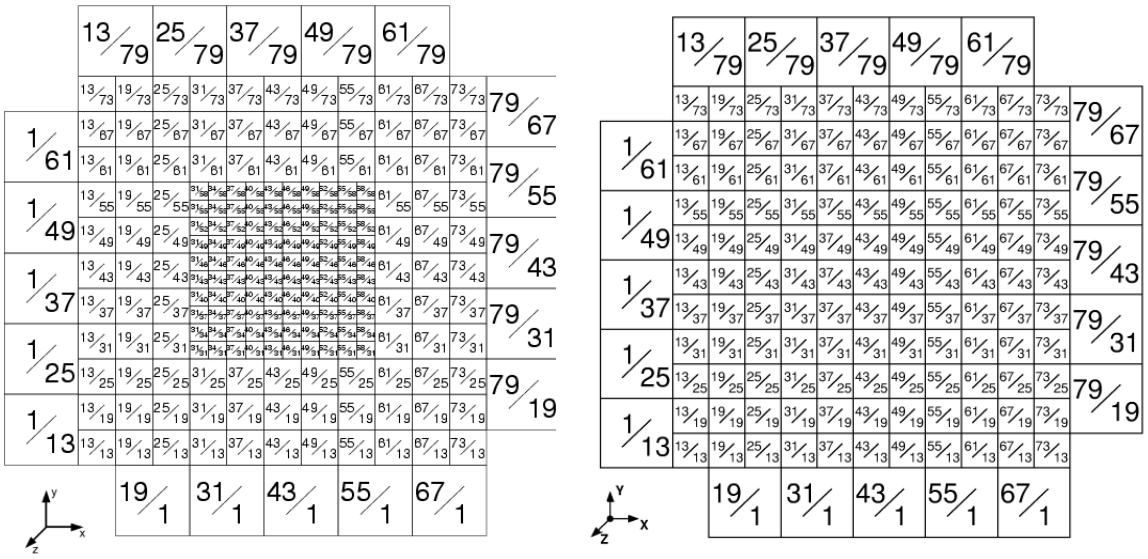

Figure 4.1: The schematic picture of AHCAL fine module (left) and course module (right). The number written in every cell are the coordinates y/x in centimeters. The zero point of the coordinate system is in the bottom left corner of layer. The coordinates for the cells are given by the coordinates of the bottom left corner of the cell.

Wavelength-shifter fibers (WLS) for transfer of photons near to the photodetector are inserted in scintillator cells. The Silicon Photomultipliers (SiPM) are used as photodetectors. All of cells in any layer are mounted in a metal casette.

As an absorber is used 16 mm steel S235. If we consider also a casette housing as an absorber (with thickness of 4 mm), the total absorber thickness is 2 cm. The total depth of calorimeter is 115 cm, what is $4.5 \cdot \lambda_0$ or $44 \cdot X_0$, where λ_0 is the interaction length and X_0 is the radiation length.

Each casette is equipped with five temperature sensors. The positions of the temperature sensors in the first two layers are along a diagonal line from the right bottom to the left top. The positions in the other layers are from the middle bottom to the middle top. Using only five temperature sensors per layer has a consequence that the temperatures for the cells have to be computed.

4.2 Silicon Photomultiplier (SiPM)

Detection of light produced by de-excitation of ionized material is made by the very new device called Silicon Photomultiplier (SiPM). The SiPMs were developed, manufactured and also tested in Russia in cooperation of three groups,

PULSAR, MEPHI and ITEP. Only the AHCAL and TCMT is equipped with SiPM photodetector.

The SiPM is a silicon-based avalanche photodetector (APD) pixelates with series of photodiodes. The number of photodiodes in one SiPM is 1156. Together they create the square of a side with length 34 pixels. The size of the area created by photodiodes is 1.1×1.1 mm^2. An example of the SiPM is shown in Figure 4.2. Each photodiode operates as $p^{++} - p - n\pi - n^{++}$ junction in Geiger mode (Fig.

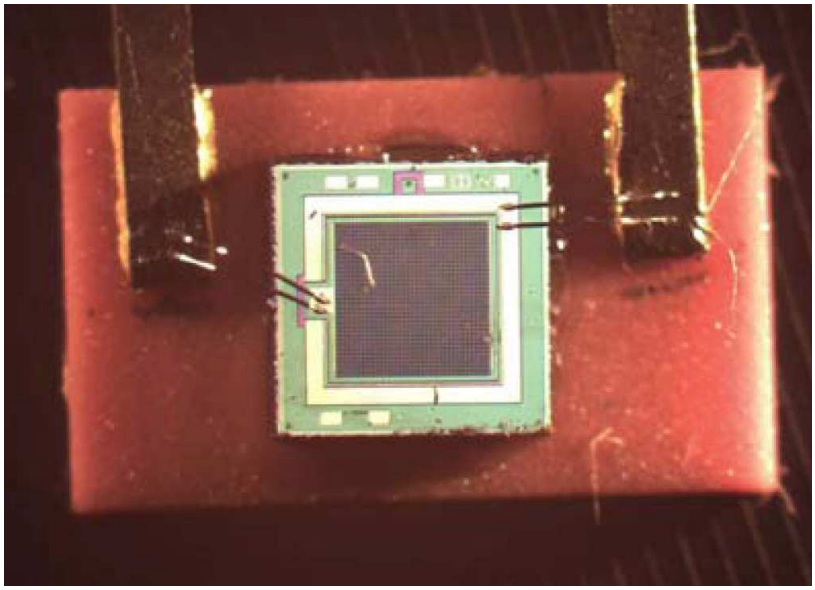

Figure 4.2: A Silicon Photomultiplier (SiPM).

4.3). A reversed voltage (U_{bias}) is applied to this p-n junction, which creates an electric field. The photons interact with silicon predominantly in the p^{++} layer where they produce the electron-hole pairs. Free electrons drift to the $p-n$ region with the highest value of the electrical field, where they have sufficient velocity of 10^7 cm/s for creating the second electron-hole pairs. The result is an avalanche of electron-hole pairs creation. The minimal applied bias voltage, which is needed to create an avalanche in the single pixel is called the breakdown voltage U_{bd}. After creating an avalanche in $p - n$ junction, electrons are drifted through the depletion region into the n^{++} part. The photodiode can produce about $10^5 - 10^6$ electrons from a single photon collision. The breakdown voltage of the SiPM is about $2.5 \cdot 10^5$ Vcm^{-1}. Bias voltages U_{bias} are between $25 - 75$ V which gives the depletion region of $1 - 3$ μm. The quenching resistors are attached parallel to the photodetectors to quench an avalanche. They have also the additional function as electrical decouplers of pixels from each others. The inter-pixel crosstalk have to be reduced also with specially designed boundaries for reduction of inter-pixel currents in the silicon itself. Since these boundaries are part of the SiPM surface,

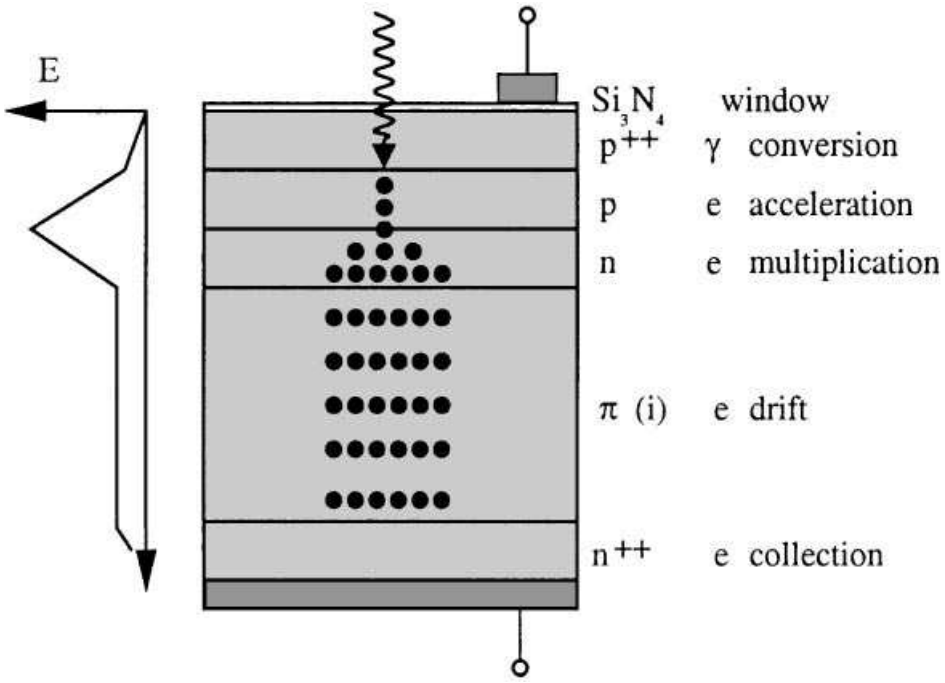

Figure 4.3: Schematic picture of the SiPMs photodiode working principle.

they reduce the sensitive area of SiPMs. The material of the quenching resistor is a polysilicon and the resistivity is in the range $R = 0.5 - 5$ MΩ. It is connected in series with a photodiode. The capacitance of each pixel is in about $C = 50$ fF. Therefore the time for one pixel to recover from discharge τ is approximately equal to

$$\tau = R \cdot C \approx 25 - 250 \text{ ns} \tag{4.1}$$

The time dependence of the signal of one SiPM pixel is shown in Figure 4.4.

A photodetector performance is influenced by an *optical crosstalk*. The probability of creation of a photon from an electron is $\sim 10^{-5}$. This number is not negligible due to high production of electrons in avalanche ($10^5 - 10^6$ electrons). The number of created electrons is sometimes called *gain*. Consequently this photon can produce another avalanche in another SiPM pixel. Probability to fire another pixel by an optical crosstalk depends on the number of fired pixels. The optical crosstalk then disturb the Poissonian distribution of the number of fired pixels.

The noise of the SiPM created by electronics is negligible in comparison with classical APDs due to high gain. The classical APD have the gain of the order 10^2. The electronics noise is smaller than 10 % of the signal from one fired pixel. The dominating source of noise is so-called *dark noise*, which is caused by free charge carriers created by thermal movement. The dark noise of the SiPM decreases with decreasing temperature. The dark noise can affect only the detection of signal

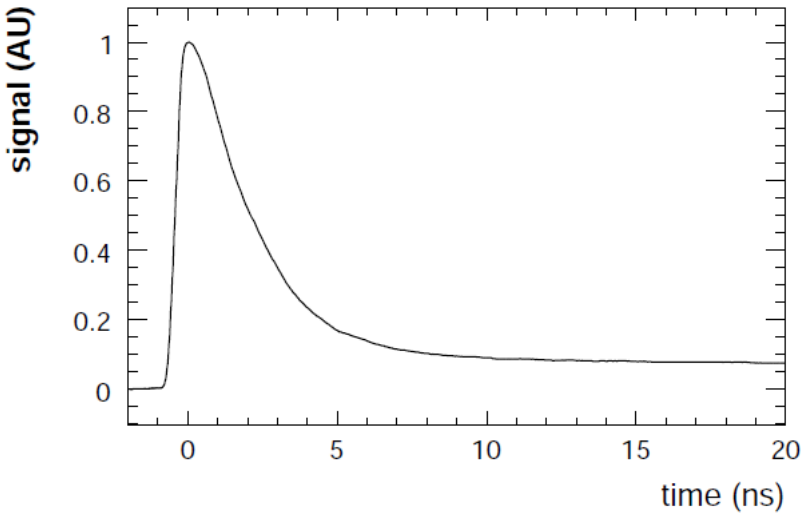

Figure 4.4: The sketch of signal shape of one SiPM pixel. [16]

created by photons with number of 10^0 in normal room temperatures. The dark noise depends linearly on bias voltage U_{bias}.

For the signal A of the SiPM holds

$$A \sim N \cdot Q_{pix}, \qquad N = 0, 1, \ldots, 1156 \tag{4.2}$$

where N is a number of fired pixels and Q_{pix} is a charge collected by the single pixel. Since the SiPM operates in the Geiger mode, the SiPM pixels is a binary-like system. As you can see from Figure 4.5, it is possible to obtain the charge of single pixel collision Q_{pix} from the distance of neighbouring peaks. The charge Q_{pix} obtained in single pixel electron-hole creation is mainly proportional to the overvoltage $\Delta U = U_{bias} - U_{bd}$ with relation $Q_{pix} = \Delta U \cdot C$.

The overvoltage is temperature depend via temperature dependence of breakdown voltage $\Delta U(T) = U_{bias} - U_{bd}(T)$. It is possible to diminish the temperature dependence of overvoltage by increasing the value of a overvoltage. The reason for temperature dependence of breakdown voltage is the smaller mean free path of electrons in the SiPM. With increasing temperature the breakdown voltage increases too. The high spread of breakdown voltage has as a consequence high spread of overvoltage. Therefore it is need to have an individual power supply of the SiPM.

Tests of SiPMs showed that the detection efficiency of the scintillator light is influenced by different independent parts and is approximately equal to 16 %. This number is a product of the quantum efficiency $\eta_{quant} = 80$ %, geometrical efficiency caused by the shape and the distance of WLS from the SiPM surface

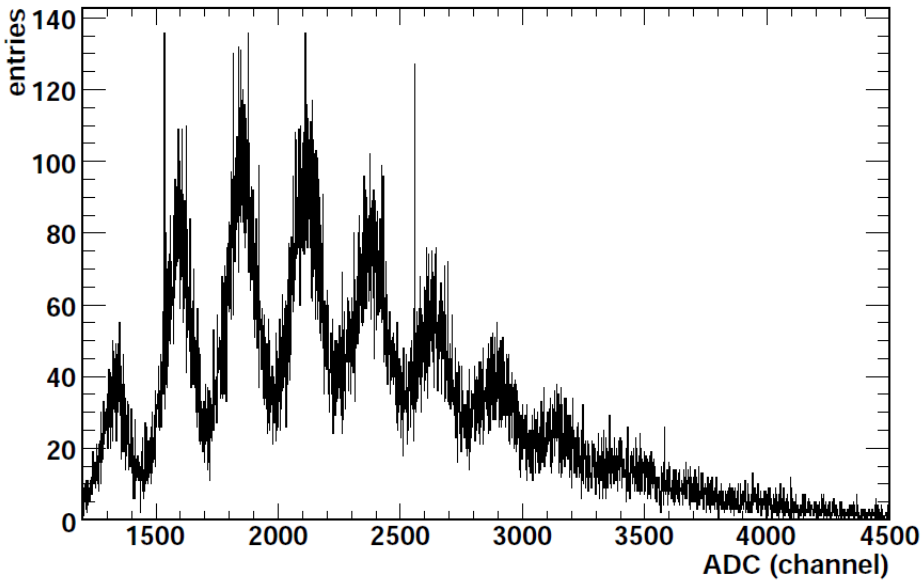

Figure 4.5: The single pixel peak distribution. [16]

η_{geo} = 20 % and the Geiger efficiency defined as a probability of creation an avalanche from the electron-positron pair which is close to η_{geig} = 100 %[11].

Nonlinearity effects of the SiPM, saturation effects

The disadvantage of SiPMs is the nonlinearity of the energy measurement which is caused by the saturation effect. This effect is more visible for the higher number of fired pixels. The saturation curves for every SiPM were measured in ITEP. The measurement of the saturation curves can be obtained also by light-emitting diodes (LEDs) from the testbeam runs. The installation of SiPMs into the calorimeter caused change of scale of the saturation curves. The rescale factor was found as 0.8, what is the ratio between the number of fired pixel from ITEP measurement and from the testbeam measurement. The difference between the measurement done by ITEP and in the testbeam is shown in Figure 4.6.

Application of rescaling parameter is one method, how to find the true nonlinearity behaviour. The other possibility is to apply any function on the testbeam measurement of SiPM response. One can simply connect measured points by a line or fit them with an analytical formula. From an obtained dependence $f(A_{in})$ of SiPMs response A_{pix} on an input light signal A_{in}, we can calculate any input signal by applying a function $f^{-1}(A_{pix})$.

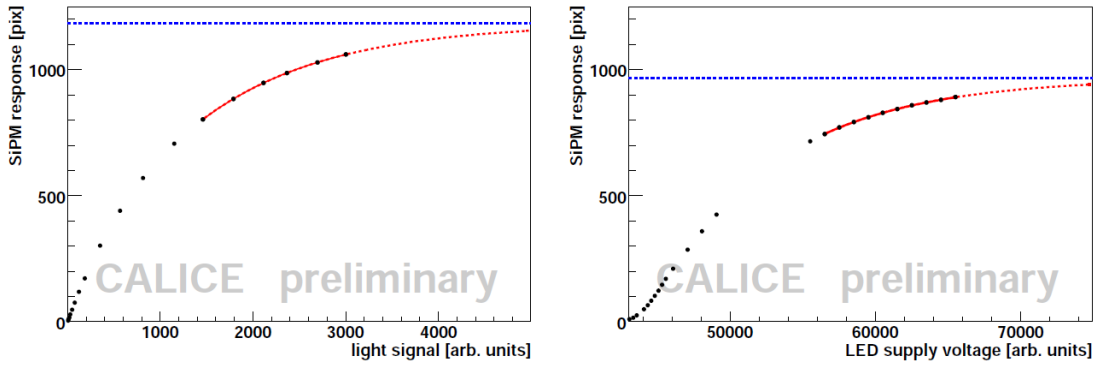

Figure 4.6: Saturation curves obtained from the measurement with LEDs as a part of the testbeam runs (left) and from the ITEP measurement (right). [13]

4.3 The Readout chain

The readout system developed for the AHCAL has the same architecture as for the ECAL. The advantage of using the same readout both for ECAL and AHCAL is the possibility of using the same data acquisition system because of the same number of readout channels. The schematic picture of the readout chain is shown in Figure 4.7. The readout starts with the signal from the SiPMs, which is amplified and shaped in the ASIC[1] chip, digitized and read in CALICE readout board.

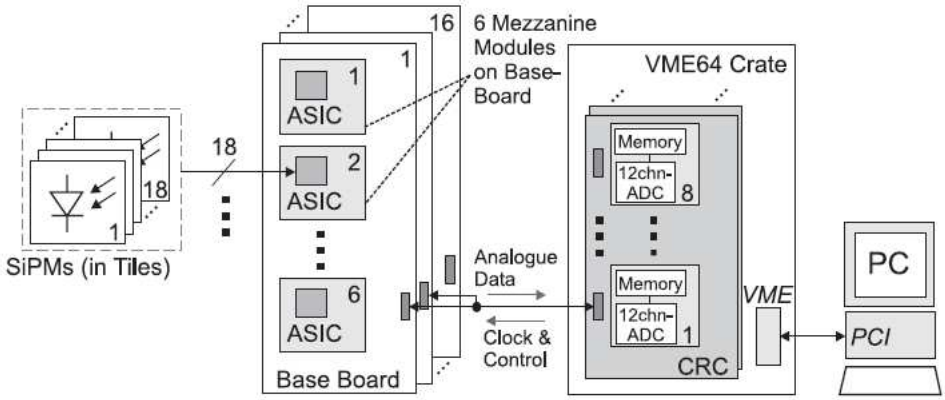

Figure 4.7: Schematic picture of the readout chain. [5]

[1] Application Specific Integrated Circuits

4.3.1 The signal processing - ASIC chips

The ASIC chips are basicaly the devices for amplification of the SiPM signal before the signal is digitized. It was built in LAL[2]. The technology used for AHCAL is the same as for ECAL prototype. The consequence of using the same ASIC chips technology is the possibility to use the same data acquisition (DAQ) for both ECAL and HCAL. The disadvantage of an amplification with ASIC chips is the loss of the shape information.

The absorbed energy E from ionisation of cells has to be proportional to the number of fired pixels, which has to be proportional to the created charge $Q_S = \int \mathrm{d}t i_S(t)$, where i_S is the current pulse of SiPM. The output of the ASIC chip as an amplifier is a voltage, which has to be also proportional to the created charge. If there would be no changing of the shape of signal in comparison with the deposited energy, the peak position of the signal would be proportional to the deposited energy. The method of determination of deposited energy by finding peak position of signal is called *pulse height analysis*.

The amplified pulse is shaped by a CR-RC^2 shaper. The pulse shape length has to be in agreement with the signal rate in the detector. Too large pulse lead to pile-up of successive pulses. After shaping the signal is held at its maximum amplitude. Such a signal is than multiplexed by an 18-channel multiplexer and sent to the Analog-Digital converter (ADC), where the analog signal is converted to the bit-pattern for subsequent digital storage and processing. The unit adc count corresponds to an input signal 76 $/mu$V. The signal processing in ASIC chip is depicted in Figure 4.8. The ASIC chips are operating in two different modes, the physics mode and the calibration mode. The shaping time is in physics mode 150 ns and in calibration mode 40 ns. An amplitude of the signal in the calibration mode is approximately 10 times higher then in physics mode. The reason for higher amplification in calibration mode is the need to resolve single pixel spectra used for the SiPM calibration by LEDs (Fig.4.5).

[2]Laboratoire de l'Accél'erateur Lin'eaire

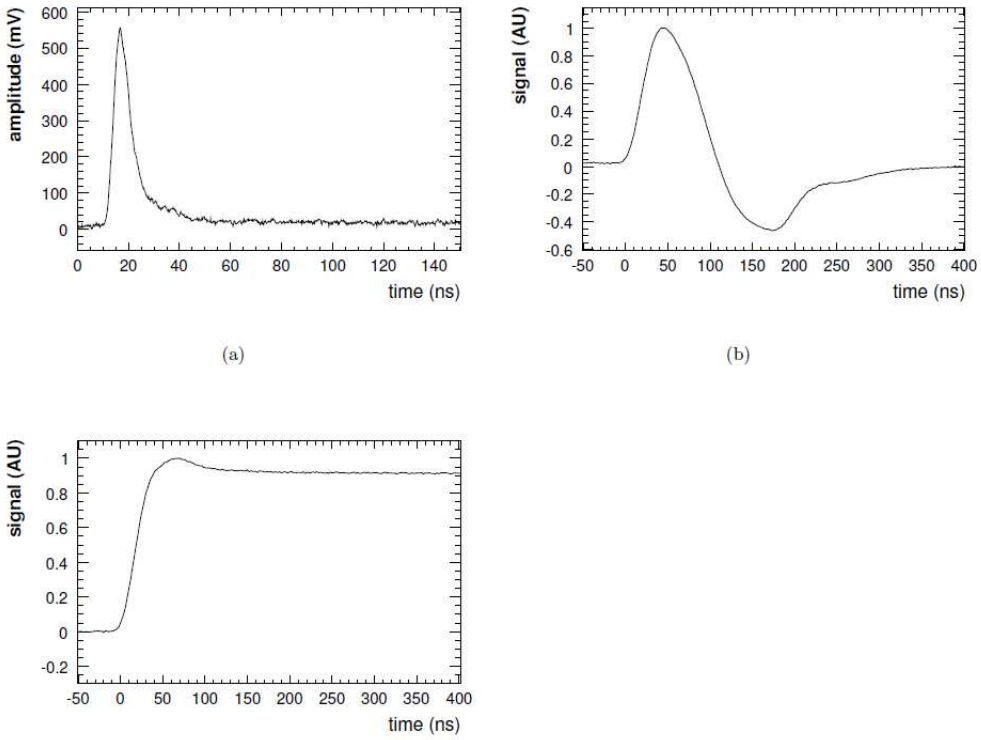

Figure 4.8: The signal processing in the ASIC. (a) an input signal, (b) amplified and shaped and held (c). [16]

Chapter 5

Software for the AHCAL analysis

The MonteCarlo simulation package *GEANT4* developed at CERN, is used for AHCAL simulations. It is implemented in the package *Mokka* with the real description of the detector parameters. The arrangement of the CALICE testbeam is also included in *Mokka*. The Mokka package was developed by the ILC community.

The important step in simulation is the digitization. It includes some detector effects obtained from experimental data, which can not be simulated like saturation of SiPM or electronics noise. There exist a lot of models for simulation of real behaviour of high energetic particles in any environment which are a good approximation of reality only in limited range of physical parameters.

The binary data from CALICE testbeams are converted to the *LCIO (Linear Collider Input Output)* format files. It is a common format for the data reconstruction (cell response equalitization, SiPM non-linearity correction, temperature correction) of all detectors for ILC. It provides both C^{++} and Java implementations. The format *LCIO* is also used for the Monte Carlo digitization.

The program *Marlin (Modular Analysis and Reconstruction for Linear Collider)* was developed to steer all of tasks for data reconstruction and analysis code based on LCIO. The input and output parameters for every task are steered by the processors. The processors have possibility to be developed, changed and chained. The chain of processors is easilly steered by the text file called the steering file.

The final analysis of data with possibility of creation plots is done in a data analysis framework *ROOT*.

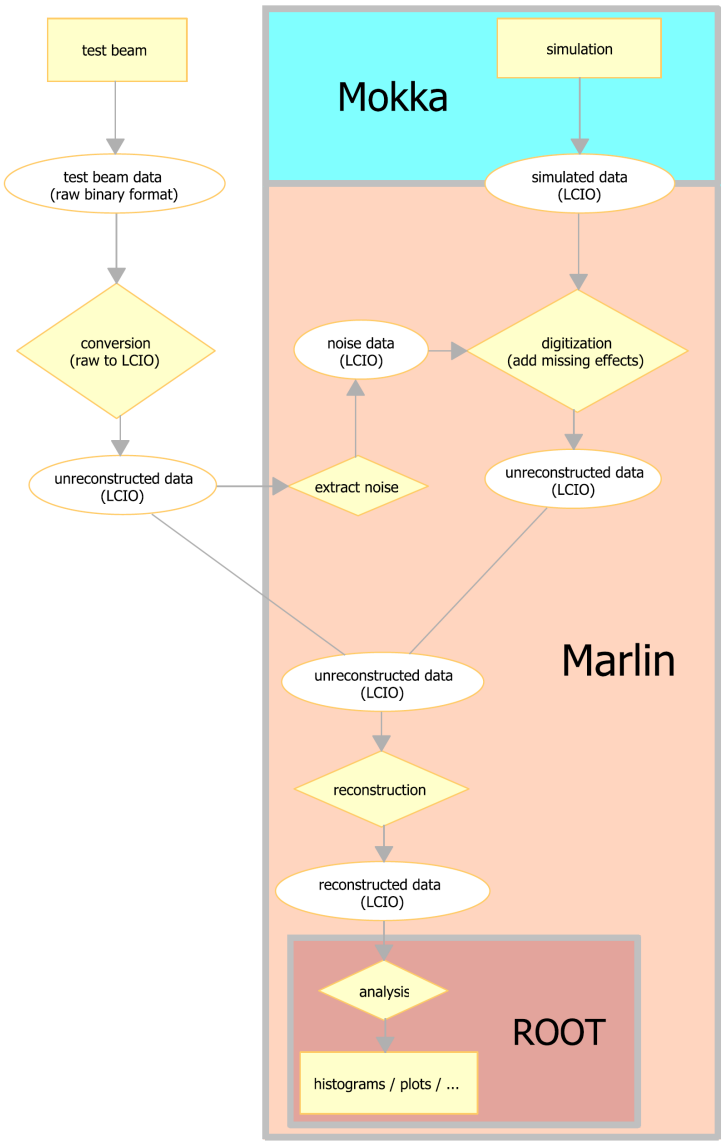

Figure 5.1: Schematic picture of the software algorithm.

Chapter 6

Calibration procedure

Calorimeter consists of about 8000 cells. These cells should have equal response to energy deposition of particles. Due to strong dependence of any other calorimeter analyse results on calibration, there is need for permanent critical view on calibration process.

The calibration procedure in physics mode is done by normalization of the signal recorded in *adc counts* to the energy deposited by a particle in the well known physical process. The particle, which was used for the calibration was muon as a minimum ionizing particle (MIP). The muons have small energy deposition by ionization in comparison with the initial energy and well described deposition of energy in calorimeter (only the ionization of environment and knocking out the delta electrons).

The SiPMs were adjusted to have the mean fired pixels per MIP approximately equal to 15. This number is also called *lightyield (LY)*.

The calibration runs were obtained from the CERN 2007 runs. The energy of muons was 80 GeV.

The calibration procedure can be done also by LEDs during runs. It gives fast information about the SiPM response.

The schematic picture of the testbeam setup for CERN 2007 is shown in Figure 6.1. In the following text is described the testbeam setup for CERN 2007 period.

The trigger system is built to make a decision about presence of a particle passing through the detector . A trigger is provided by coincidence of scintilator plates. The size of scintilator plates is 10×10 cm^2, 20×20 cm^2 and 100×100 cm^2.

The Cherenkov counter is a long tube filled with a helium gas. It is used for a discrimination of electrons from pions. The emitted light from particles transversed through the gas is detected and multiplied by *Photomultiplier Tube*.

Drift chambers are used to find the position of transversed particle. A strong electrical field causes a drift of free electrons created by the ionisation of gas.

Electrons are collected on the sides of the drift chamber. The time of the drift to the sides is proportional to the position of the particle.

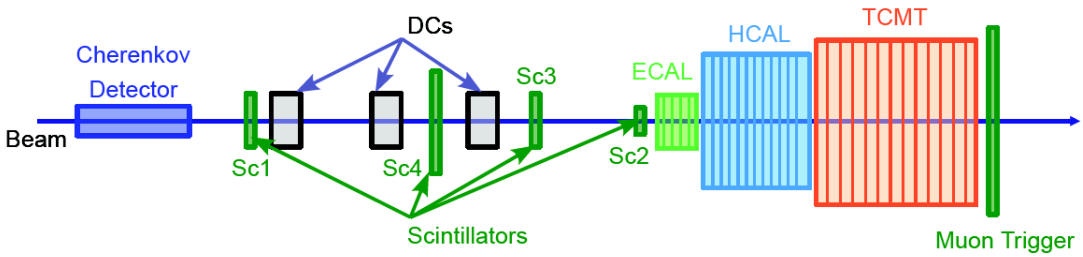

Figure 6.1: The testbeam setup for CERN 2007 runs. Sc means scintillator counter which serves as trigger, DC means drift chamber serves for reconstruction of the incoming particle position. Cherenkov detector serves for the particle identification.

Distribution of the cell response A_{MPV} of muons for all of cells measured in adc counts is shown in Figure 6.2. The spread of A_{MPV} is too large so the cell equalitization factor has to be measured for every cell. The cell response or the cell equalization factor A_{MPV} is the most probable value (MPV) of deposited energy of muons passing through the cell. The unit of the energy deposition after the calibration is the multiplicity of obtained A_{MIP}. The energy is then written in so-called MIP units.

Various muon calibration methods have been already applied for the muon runs. The emergency of calibration problem for the cells with a low statistics demands another method which could solve this problem. We have developed and applied the another calibration method to data which is also suitabe for the cells with a small statistics.

Energy of high energetic muon is mainly deposited in a cell by ionization, which is well described by a probability formula of energy deposition ϵ in the material of length x, invented by L.N. Landau [19].

$$l(\xi(x), \epsilon) = \frac{\theta(\lambda(\epsilon, \xi))}{\xi}, \tag{6.1}$$

where $\xi(x)$ is for of relativistic muons equal to

$$\xi(x) = 0.1535 x \frac{\rho Z}{A\beta^2}. \tag{6.2}$$

Z is an effective proton number of a material. The function $\theta(\lambda)$ is expressed as

$$\theta(\lambda) = \frac{1}{2\pi} \int_{K-i\infty}^{K+i\infty} \mathrm{du}\ \exp[u \ln u + \lambda u] \tag{6.3}$$

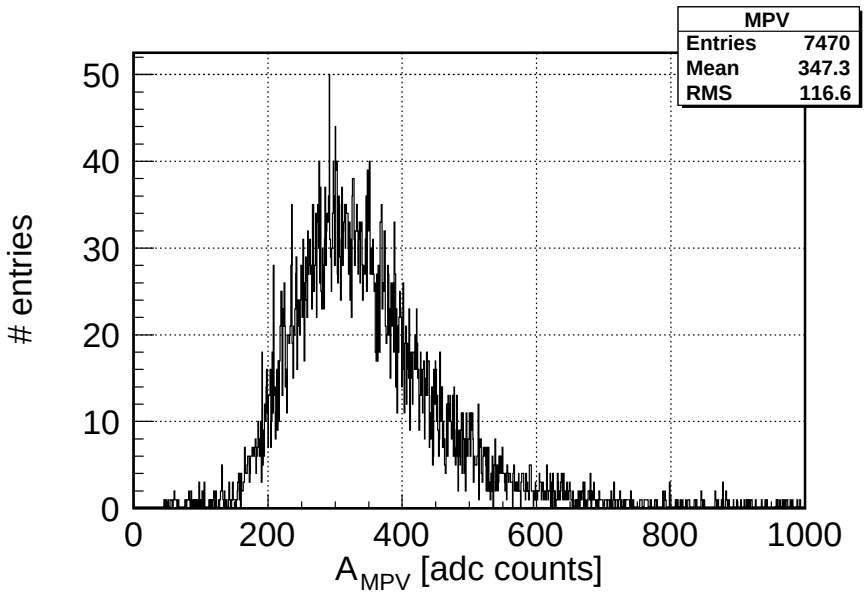

Figure 6.2: Distribution of cell equalization factors extracted as the MPV of energy deposited by 80 GeV muons in each cell. (Data from CERN 2007 run).

where K is any positive constant.
For *Full Width at Half Maximum (FVHM)* holds $FWHM \approx 4.02\xi$. The last parameter λ can be written as

$$\lambda(\epsilon, \xi) = \frac{1}{\xi}\left(\epsilon - \langle\epsilon\rangle\right) - \beta^2 - \ln\left(\frac{\xi}{W_m}\right) - 1 + C_E \tag{6.4}$$

where C_E is Euler constant and W_m is maximal transfered energy in a single collision.

Only a Landau function $l(x, \epsilon)$ is not sufficient to describe measured energy distribution because the energy is smeared by electronic noise. This smearing is approximately described by a Gaussian distribution $g(\epsilon)$. Since the deposition of energy in the cell and electronics smearing are independent we can compute the final distribution like a convolution:

$$(l \otimes g)(\epsilon) = \int \mathrm{d}\epsilon'\ l(\epsilon - \epsilon')g(\epsilon')^1 \tag{6.5}$$

Ideally one would have to include also the Poissonian statistic introduced by the SiPM response, but this would complicate the fit and make it considerably slower. We assume instead that the Gaussian function will absorb also the Poissonian fluctuations. This assumption is checked in Figure 6.7. The reason for using

[1]The Landau distribution is included in the analysis package ROOT in a class *TMath*.

smaller number of parameters is also the correlation of parameters (Fig. 6.3).

The parameters which we get from fitting process are

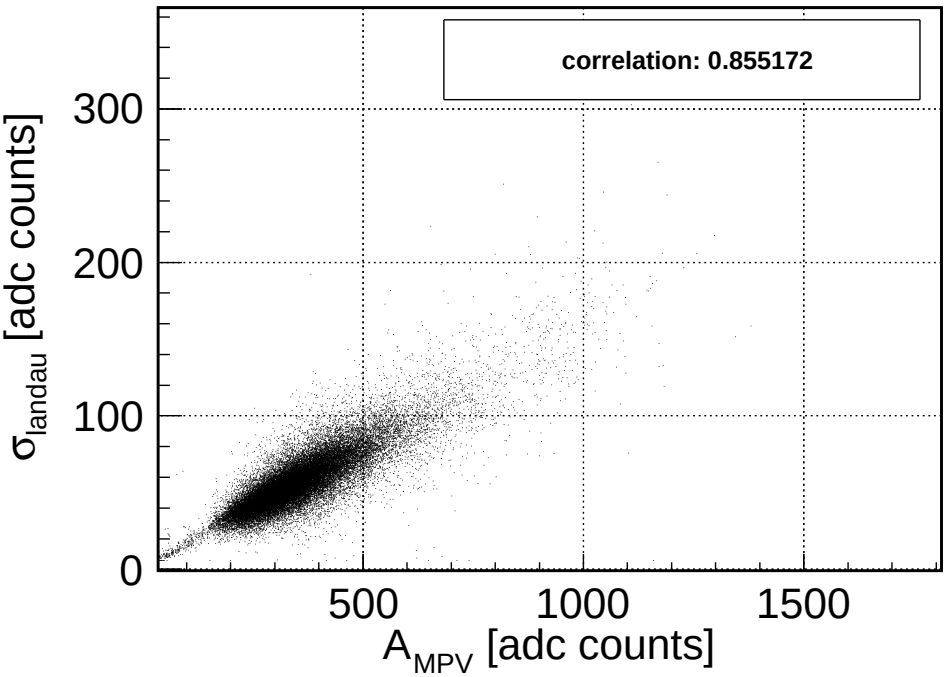

Figure 6.3: Correlation between sigma of the Landau function σ_{landau} and A_{MPV}.

- the mean of the Landau distribution (Landau mean)
- the sigma of the Landau distribution (Landau sigma)
- the sigma of the Gauss distribution (Gauss sigma)

The mean of the Gaussian distribution is fixed at the zero value. We are mostly interested in the most probable value (MPV) of deposited energy or the highest value of the distribution function (6.5), which we have to compute numericaly. The mean of deposited energy is a more realistic value but we can see in the muon energy spectrum a remaining contribution of pedestal events around zero. Ideally only true muon energy depositions should be filled in the energy distribution histogram. In this way no exccess at zero is expected. The energy distribution histogram with excess on zero is shown in Figure 6.5 (left). Those events are due to inefficiency of the track finder in identigying which calorimeter cell is traversed by the muon track in each event, i.e. inclined tracks traverse cells in two adjacent

towers in the calorimeter geometry. More details on the track finding algorithm are given in chapter 8. If there would be no electronics smearing, the pedestal

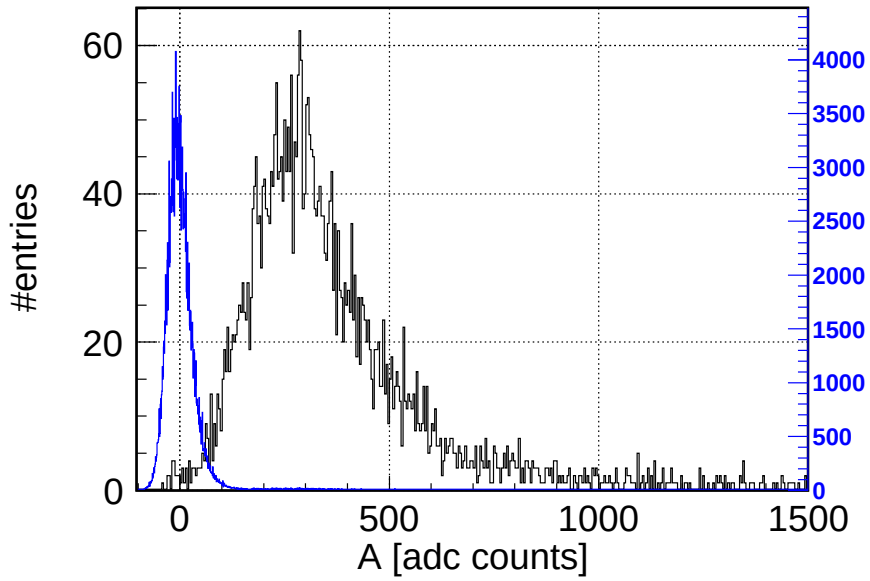

Figure 6.4: The comparison between the distributions of deposited energy of muons and of pedestal (blue color).

would have the delta-like function distribution. The mean value of this function would define the zero point or value of zero deposition of energy. This zero value is obtained by so-called "on the fly" method, where the random events are taken between triggered good events (in our case the muon events). Then the mean of pedestal events is computed from N pedestal events, which is assumed to be the zero point. The number of random events N is the steering parameter of a Marlin processor (see chapter 5). A representative histogram with the mean of pedestal events at zero is shown in Figure 6.4.

6.1 Likelihood fit

The method previously used for estimation of fitting parameters was the traditional χ^2 *method*. We have developed a modified method based on the *maximum likelihood fit*.
Let us quickly to describe both methods.
χ^2 fitting method:
Let us assume, that we have set of values X (equidistant bins of histogram), for which we measure any other set Y. Let us also assume, that we have any functional

expression for image of set X to Y:

$$y_i = f(x_i)\ x_i \in X,\ y_i \in Y \tag{6.6}$$

Notice, that here the number of entries of histogram is $\sum_{y_i \in Y} y_i$. Let's have function of parameters β, $\hat{Y} = f(\beta|X)$, where $\hat{Y}$ is so called estimator of Y. For finding the best estimator $\hat{Y}$ of Y we minimize the "distance" of "vectors" Y and $\hat{Y}$:

$$\|Y - \hat{Y}\|^2 = \chi^2 = \sum_i (y_i - f(\beta|x_i))^2 \quad y_i \in Y\ x_i \in X \tag{6.7}$$

If we know also the sigma of y_i, σ_i, which is assumed to be gaussian for sufficiently high value of y_i, we can weight the distance by $1/\sigma^2$:

$$\chi^2 = \sum_i \frac{(y_i - f(\beta|x_i))^2}{\sigma_i^2} \tag{6.8}$$

likelihood fitting method:
Let's assume, that X is measurement set of random variable x with probability function $f(\beta|x)$. Notice, that here the number of entries in our histograms is the number of x_i; $x_i \in X$. The estimation of parameters β is based on maximizing probability $L(\beta)$ to get set X:

$$L(\beta) = \prod_{x_i \in X} f(\beta|x_i) \tag{6.9}$$

There is a very fine but crucial difference between these two methods. The fitting process of χ^2 method includes also zero bins of histogram of the deposited energy. The consequence is that the fit gives unreliable results for cells with low statistics. On the other hand, the likelihood method can be efficiently used for cells with low statistics (Figure 6.5).

6.2 Fast Fourier transformation (FFT)

The fitting process of χ^2 method is based directly on equation (6.5), where the integral was evaluated by discretization

$$\int_{-\infty}^{\infty} \mathrm{d}\epsilon'\ l(\epsilon - \epsilon')g(\epsilon') \to \Delta\epsilon' \sum_{i=-N}^{N} l(\epsilon - i\Delta\epsilon')g(i\Delta\epsilon') \tag{6.10}$$

where $\Delta\epsilon' \to 0$, $N \to \infty$ and $g(N\Delta\epsilon') \to 0$. Some good cells have very low values of the Landau sigma as it is shown in Figure 6.3. The result is very narrow Landau function in the fitted convolution function. The same problem is also emerging in the case of a small sigma of a Gaussian function.

$$(l \otimes g)(\epsilon) \to g(\epsilon) = \int_{-\infty}^{\infty} \mathrm{d}\epsilon' \delta(\epsilon - \epsilon')g(\epsilon'), \tag{6.11}$$

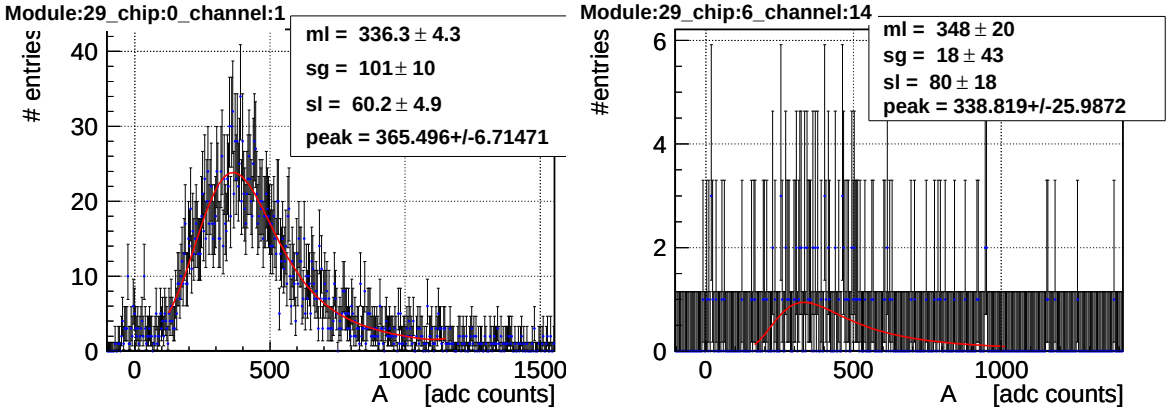

Figure 6.5: Deposited energy of muons with high (left) and low (right) statistics, fitted with a function defined as a convolution of the Gaussian and the Landau function (used likelihood method). The excess of distribution in zero is visible in the left histogram.

or

$$l(\epsilon) \to \delta(\epsilon) \qquad \sigma_{landau} \to 0 \tag{6.12}$$

Therefore the fitting function evaluated according to (6.10) is sometimes not appropriate as it is visible in Figure 6.6. We have solved this disadvantage by applying the discrete Fourier transformation on our data set. One important feature of Fourier transformation is

$$\mathcal{F}(\delta) = \text{const} \tag{6.13}$$

With the help of this equation we have solved a problem of a small Landau or a Gaussian sigma parameters.

The problem of fitting the histogram of deposited energy by muon events is shown in Figure 6.6, where on the right side is the fitted histogram using the method based on (6.10) and χ^2 method and on the right side is the fitted histogram using the FFT and also likelihood method.

For fitting our data sets we have used the analysis framework *ROOT*, specially the library *RooFit*. For computation of FFT we have used the library *FFTW3*.

6.3 Results of muon calibration

For calibration procedure we use muon runs from CERN 2007 run period with run numbers from 330254 to 330258. All of this runs are merged in one run because of the same voltage settings and approximately same temperature. These set of runs were also used for χ^2 method fits. It gives us a possibility to compare both procedures.

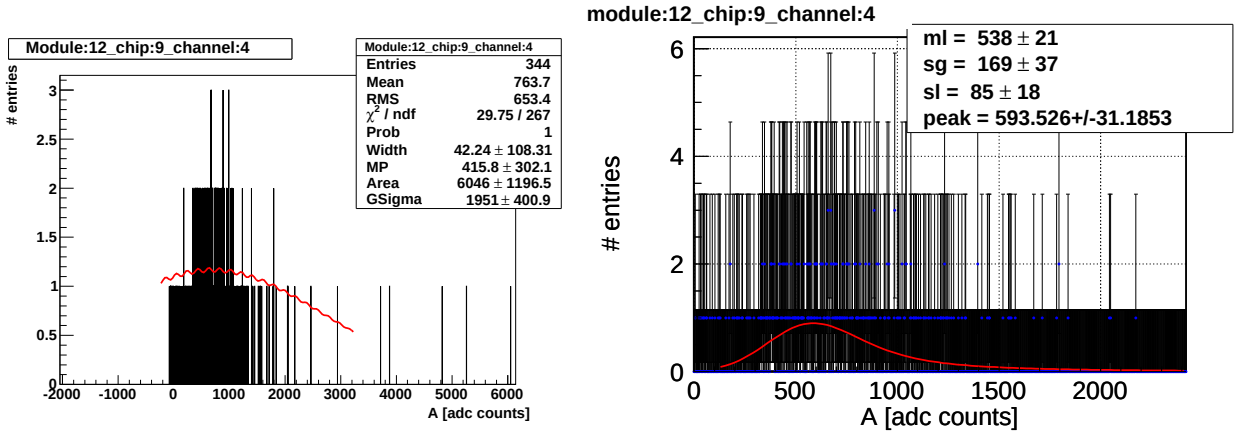

Figure 6.6: Deposited energy of muons for the low statistics fitted with a convolution function (6.5) created by method which is based on the equation (6.10) and by χ^2 fit method (left) and with a convolution function created by FFT method and by likelihood fit method (right). The both histograms have the same binning.

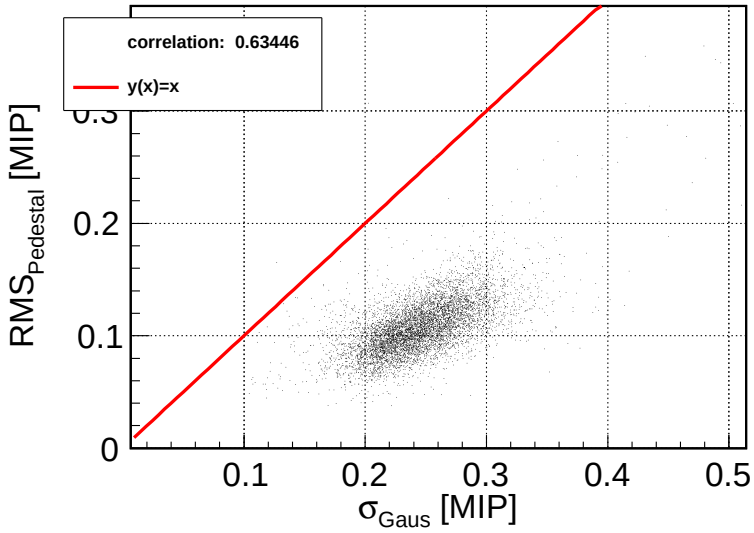

Figure 6.7: The correlation between RMS of pedestal distribution from pedestal part of runs $RMS_{pedestal}$ and the sigma of the Gaussian part of a fitting function σ_{Gaus} defined by (6.5). The values are expressed as multiples of MIP.

Before the comparision of both methods we have to check the consequence of avoiding the Poissonian statistics of the SiPM response. In the introduction of this chapter the assumption has been made that the Gaussian function would incorporate also the Poissonian smearing coming from the SiPM intrinsic response. If this is true the resulting value of the Gaussian sigma is expected to be larger than the true pedestal width, but still correlated to it. This is consistent with Figure 6.7.

The correlation of results of both methods can be characterised by the shift defined as

$$P_{a,b} = 2 * \frac{A_a - A_b}{A_a + A_b}, \tag{6.14}$$

where $A_{a(b)}$ is the position of most probable value of method $a(b)$.

Histogram on the right side of Figure 6.8 is the distribution of the MPV shift defined like $P_{likelihood,\chi^2}$. The mean of the distribution is 0.03. The correlation of MPVs per cell of the likelihood method and the χ^2 method is shown on the left side in Figure 6.8. The correlation factor is 0.994. We can concluded, that χ^2 and *likelihood* fitting methods are very good correlated but they are biased to each other.

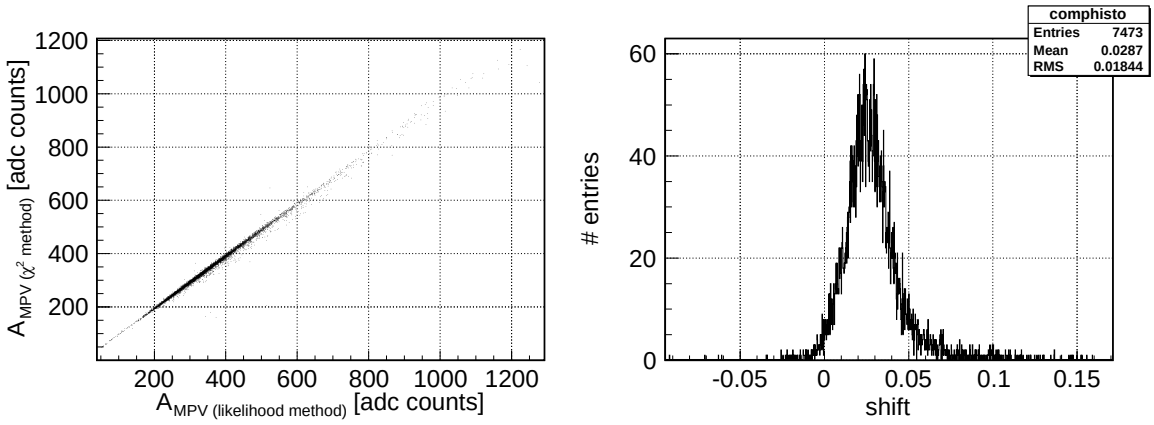

Figure 6.8: Correlation of MPV per cell of the likelihood method and the χ^2 method (left). Distribution of shift $P_{likelihood,\chi^2}$, defined by (6.14) (right).

Which one is less biased in the evaluation of MPV? It is possible to answer that question because MPV is a quantity, which one can roughly get from a data set without knowledge of physically derived distribution. Finding the MPV from data set was done by smoothing the histogram of deposited energy with *running average*. Such a peak finding is not precise, but we can expect that it is not biased. This method is called further as *rough method*. The distributions of quantities $P_{\chi^2,rough}$ and $P_{likelihood,rough}$ for every cell is shown in Figure 6.9. The summary of results is written in Table 6.1. It is obvious, that likelihood method is negligible biased in comparison with χ^2 method.

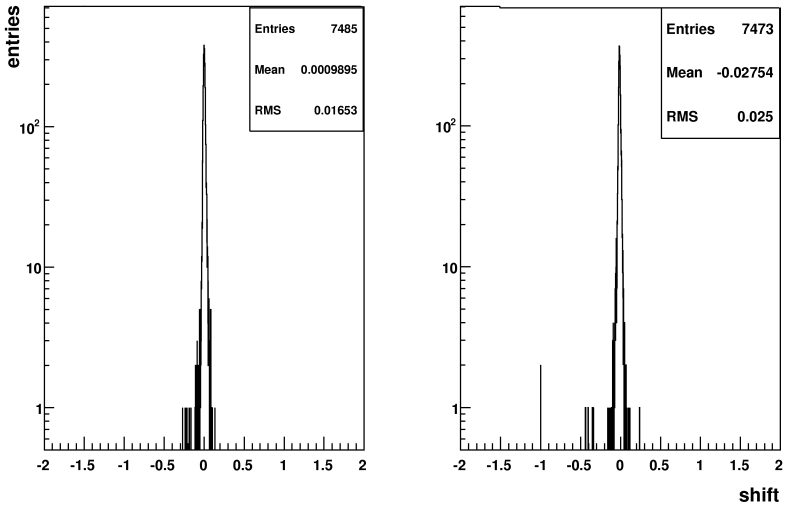

Figure 6.9: The distribution of shift $P_{likelihood,rough}$(left) and $P_{\chi^2,likelihood}$ (right) defined by (6.14) for every cell.

shift	mean	rms
$P_{likelihood,\chi^2}$	0.029	0.018
$P_{likelihood,rough}$	0.001	0.017
$P_{\chi^2,rough}$	-0.028	0.025

Table 6.1: The comparison of χ^2, likelihood and rough methods using the equation (6.14).

To quantify the stability of fitting process we have used separately five runs with numbers 330254-330258. We have changed the range of fit and binning of a data set. We have computed A_{MPV} for every combination of used ranges and binnings. For every cell we have computed the mean $\langle A_{MPV} \rangle$ from all A_{MPV} for fixed range (binning). The value, which we have computed is

$$D(A_{MPV}) = 2 * \frac{A_{MPV} - \langle A_{MPV} \rangle}{A_{MPV} + \langle A_{MPV} \rangle}. \tag{6.15}$$

The results are shown in Figure 6.10. The stability is mainly disturbed by changing of range where the deviation of A_{MPV} is in about 1.5%. Better results for stability of the likelihood fit are obtained for smaller binning.

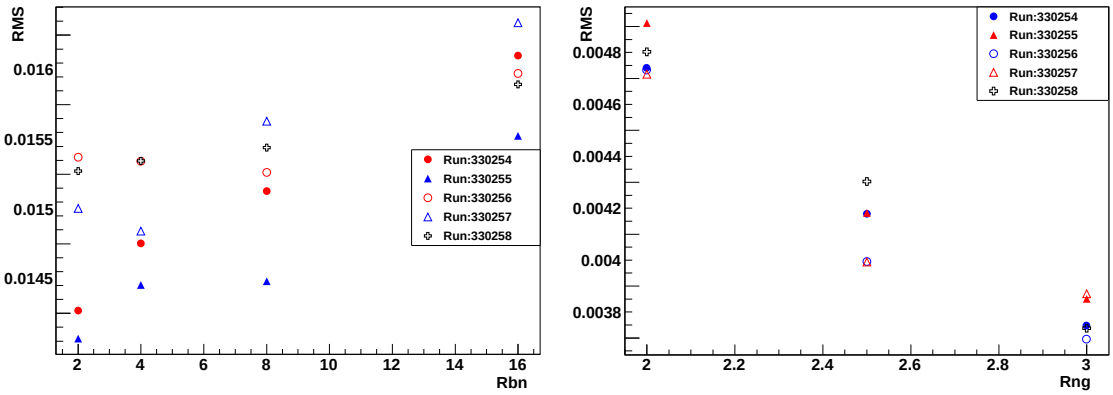

Figure 6.10: The RMS of distribution of quantity $D(A_{MPV})$ defined by (6.15) for changing a binning (left) and range (right). The quantity Rng is the positive number for the range definition $< min, A_{MPV} \cdot Rng >$. The range is obtained iteratively. From the first fit it is found roughly the A_{MPV}. Than there is adjusted the range as $< min, A_{MPV} \cdot Rng >$. The value of binning Rbn means, how many bins are added together.

6.3.1 Summary of results

We have developed a new method for fitting the deposited energy of muons. The problem of small entries of some cells (Fig. 6.5) has been solved by application of the likelihood fitting method. The problem of evaluation of convolution function (6.5) (Fig. 6.6) has been solved by application of the FFT. The results of the modified fitting method are biased with the results of the default fitting method (Fig. 6.8). The validation of the modified fitting algorithm is made by the comparision of obtained A_{MPV} with the rough method results (Tab. 6.1). The study of fitting stability (Fig. 6.10) shows the stability of fit in about 1.5 % by changing of the range of fit.

Chapter 7

Temperature and voltage dependence of deposited energy

Since the SiPM is sensitive to changes of temperature T and bias voltage V, the dependence of the cell response on T and V has to be determined and used as a correction in the data analysis. These dependences have been determined from all CERN 2007 runs and also from FNAL 2008 runs. Used muons from CERN 2007 runs have energy of 80 GeV, muons from FNAL 2008 runs have energy of 32 GeV. To check the voltage dependence of SiPM, there are four values of voltages setting per cell, both for CERN 2007 and FNAL 2008 runs. The information about the energy of the beam is accessible from so-called electronic logbook (elog book). The information of bias voltages and temperatures were recorded in the slow control every 10 minutes. Spread of voltage for one run is negligible, maximal deviation from mean voltage is 20 mV. We have used only muon runs where the beam is perpendicular to layers of the calorimeter.

For finding temperature and voltage dependences, we could not merge CERN 2007 and FNAL 2008 runs straightforward due to different energies of beams.

7.1 Temperature and voltage slopes

The temperature and voltage dependence of the most probable value $A_{MPV}(T,V)$ of deposited energy in muon runs has been parametrized as

$$A_{MPV}(T,V) = A_{MPV}(T_0,V_0) + \frac{dA_{MPV}}{dT}(T_0,V_0)(T-T_0) + \frac{dA_{MPV}}{dV}(T_0,V_0)(V-V_0), \tag{7.1}$$

where we have ignore higher order terms. The mixed term $P_{VT} \cdot (V-V_0)(T-T_0)$ was also neglected because the low statistics of the measurement gives a big uncertainty of the fitted parameter P_{VT}. The quantities $\frac{dA_{MPV}}{dT}(T,V)$ and $\frac{dA_{MPV}}{dV}(T,V)$ are assumed to be constant. The reason is following. The amplitude

of the signal A_{MPV} is assumed to be proportional to the charge created in the SiPM

$$Q = NQ_{pix} = NC_{pix}(U_{bias} - U_{bd}). \tag{7.2}$$

All of quantities are described in section 4.2. An applied bias voltage is in this chapter signed as V instead of U_{bias}. It holds for the temperature and voltage slopes

$$\frac{dA_{MPV}}{dT}(T,V) \sim \frac{dU_{bd}}{dT}\frac{dA_{MPV}}{dU_{bd}} = -NC_{pix}\frac{dU_{bd}}{dT} \tag{7.3}$$

$$\frac{dA_{MPV}}{dV}(T,V) \sim NC_{pix} \tag{7.4}$$

The dependence of U_{bd} on the temperature for MPPCs[1] in [14] shows a linear trend for the temperature dependence of U_{bd} with $\mathrm{d}U_{bd}/\mathrm{d}T = 56 \pm 0.1$ mV/K.

The slopes have been determined for the CERN 2007 and FNAL 2008 runs. The method which was used previously was based on the two independent linear fits of the slopes. The first linear fit was applied for the determination of the temperature slopes. The voltage slopes were consequently determined with applied temperature corrections.

We have tried to modify the method to increase the stability of slopes determination. Both methods exploit the observation of collinearity of temperature slopes at the different voltages.

- A combined fit of the two data sets has been performed to extract a common slope on a larger temperature range, though allowing for the two data sets to have a common offset due to the difference in muon energy at the two testbeams.

  The linear fit of CERN 2007, FNAL 2008 and merged linear fit is shown in Figure 7.1. The method of merging data sets improved the statistics. Unfortunately there were some cells where the assumption of the same temperature slopes for the CERN 2007 and FNAL 2008 runs was not fulfilled.

- The second modification also exploit the assumption of the same temperature slopes for the various voltages. It consists of the application of a planar fit on $A_{MPV}(T,V)$, what means using the other voltage settings of the SiPMs. From such a planar fit we could also find the voltage dependence of $A_{MPV}(T,V)$. The picture of planar fit of $A_{MPV}(T,V)$ and a projection of this plot for the nominal voltage is shown in Figure 7.2.

The same method of merging CERN 2007 and FNAL 2008 data can be used also for planar method. The consistency of the fit of both data sets can be calculating the ratio $A_{MPV}(\langle T\rangle, \langle V\rangle)_{CERN}/A_{MPV}(\langle T\rangle, \langle V\rangle)_{FNAL}$. Here $\langle T\rangle$ and $\langle V\rangle$ are the means of all temperature and voltage values. The ratio should correspond to the

[1] Multi-Pixel Photon Counter.

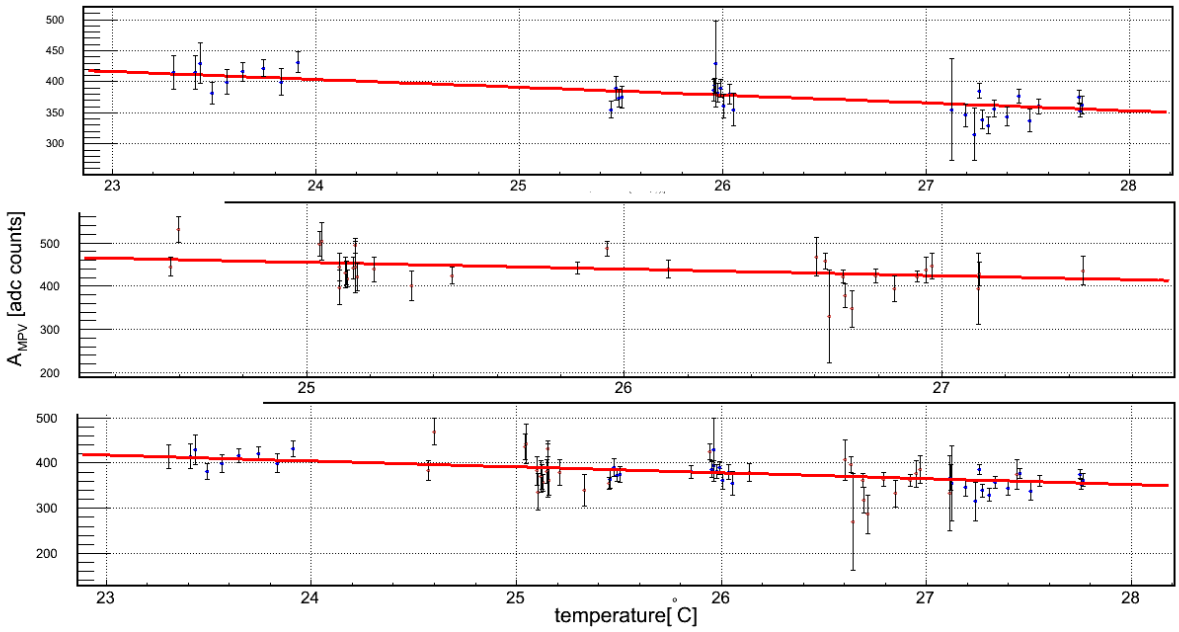

Figure 7.1: Linear fit of temperature slopes for CERN 2007, FNAL 2008 runs and merged linear fit described in text.

ratio of the mean energy losses of muons in both run periods. Since the energy of muons in CERN 2007 runs (80 GeV) is bigger than in FNAL 2008 runs (32 GeV), the ratio has to be bigger than one. It is clear that this distribution correspond to the expected ones.

The distributions of $A_{MPV}(\langle T\rangle, \langle V\rangle)_{FNAL} - A_{MPV}(\langle T\rangle, \langle V\rangle)_{CERN}$ and $A_{MPV}(\langle T\rangle, \langle V\rangle)_{CERN}/A_{MPV}(\langle T\rangle, \langle V\rangle)_{FNAL}$ are shown in Figure 7.3.

7.2 Results of temperature and voltage slopes

7.2.1 Temperature slopes for individual cells

The correlation of the slopes obtained by old (line) and new method (planar) for the CERN 2007 runs is shown in Figure 7.4. The correlation factor is not satisfactory, what can be caused by the uncertainty of the line fit parameters.

The quality of the line and planar method can be estimated by the comparison of the distribution of $|\sigma_{slope}/slope|$, where σ_{slope} is the slope uncertainty obtained from fit. The distribution of $|\sigma_{slope}/slope|$ is shown in Figure 7.5 and 7.6 for the CERN 2007 and FNAL 2008 runs. It is obvious that a slope for the planar fit method gives significantly smaller uncertainties. The uncertainty of the slopes for FNAL 2008 runs is better, but not so significantly as for CERN 2007 runs.

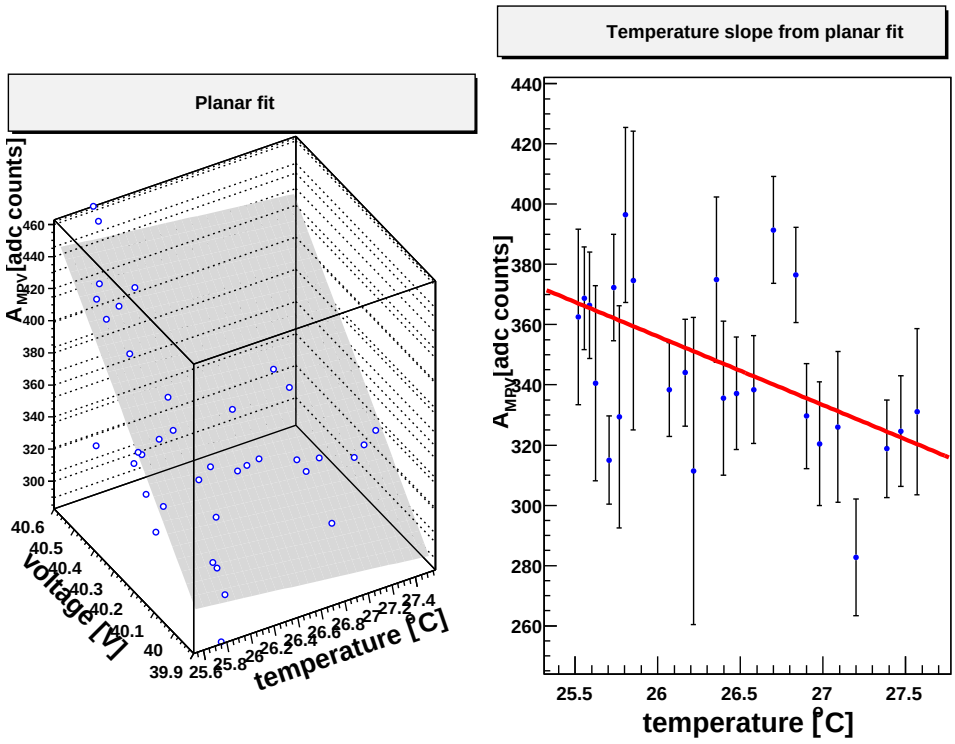

Figure 7.2: Left: The most probable value of deposited energy A_{MPV} as a function of temperature and voltage. The grey area represents the result of the planar fit. Right: The dependence of A_{MPV} on temperature at the nominal voltage. The line represents the result of the planar fit.

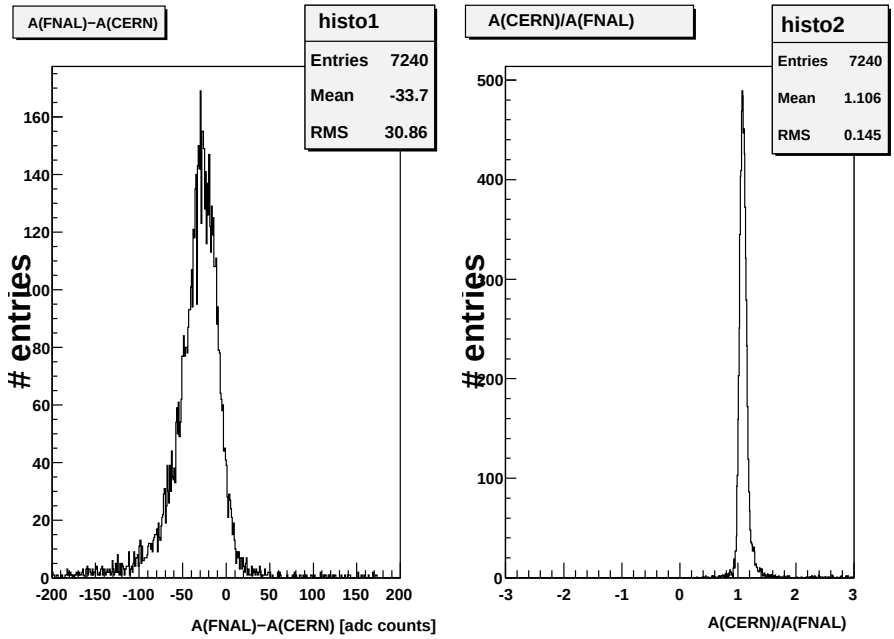

Figure 7.3: Distribution of $A_{MPV}(\langle T\rangle, \langle V\rangle)_{FNAL} - A_{MPV}(\langle T\rangle, \langle V\rangle)_{CERN}$ and $A_{MPV}(\langle T\rangle, \langle V\rangle)_{CERN}/A_{MPV}(\langle T\rangle, \langle V\rangle)_{FNAL}$. The value of $A_{MPV}(\langle T\rangle, \langle V\rangle$ is obtained from fit.

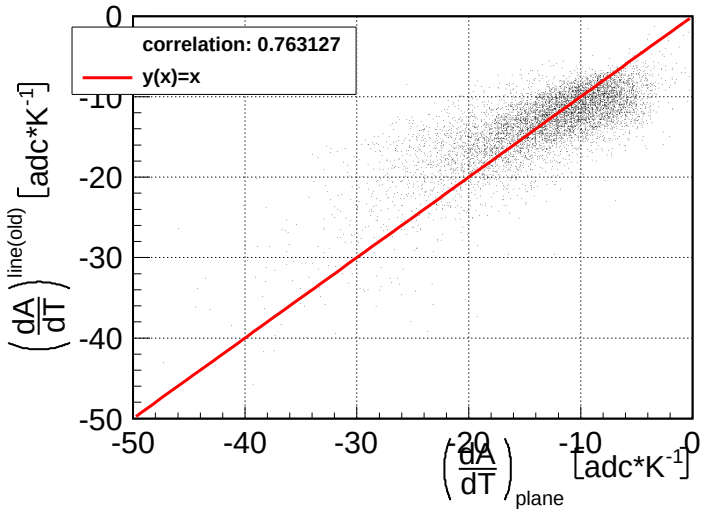

Figure 7.4: Correlation of the slopes obtained by the old line and planar methods.

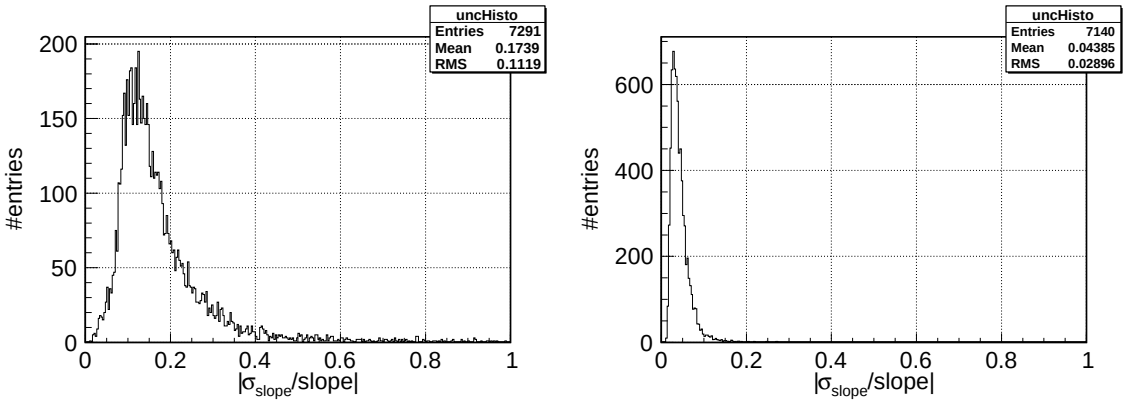

Figure 7.5: The distribution of relative uncertainties of the temperature slopes $|\sigma_{slope}/slope|$ for the line (left) and planar (right) method. Used CERN 2007 runs.

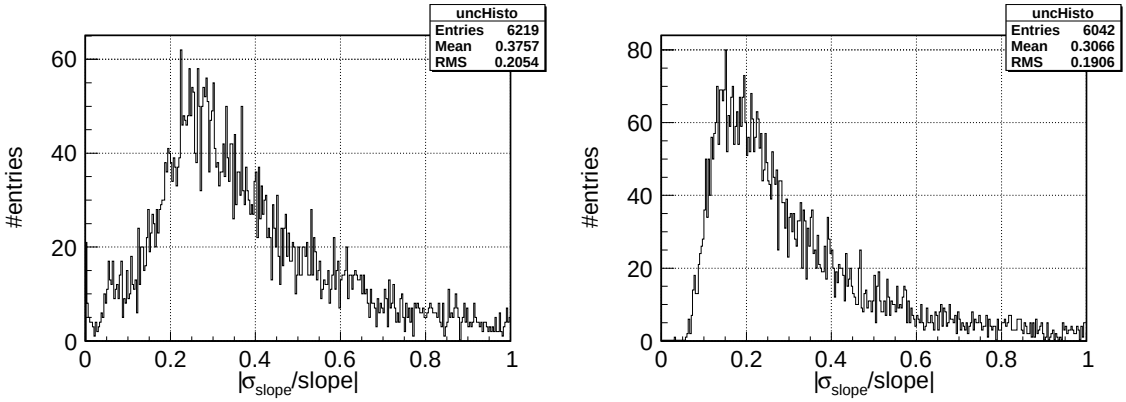

Figure 7.6: The distribution of relative uncertainties of the temperature slopes $|\sigma_{slope}/slope|$ for the line (left) and planar (right) method. Used FNAL 2008 runs.

7.2.2 Temperature and voltage characteristic for all cells

The temperature and voltage characteristic of cells which is not depend on the SiPM itself can be written as

$$K_T = \frac{1}{\langle A_{MPV} \rangle} \frac{\mathrm{d}A_{MPV}}{\mathrm{d}T} \qquad K_V = \frac{1}{\langle A_{MPV} \rangle} \frac{\mathrm{d}A_{MPV}}{\mathrm{d}V} \tag{7.5}$$

These quantities are assumed to be the same for all of cells. It can be derrived using equation (7.2):

$$\frac{1}{A_{MPV}} \frac{\mathrm{d}A_{MPV}}{\mathrm{d}V} = \frac{1}{V - U_{bd}} \tag{7.6}$$

$$\frac{1}{A_{MPV}} \frac{\mathrm{d}A_{MPV}}{dT} = \frac{-\mathrm{d}U_{bd}}{dT} \frac{1}{A_{MPV}} \frac{\mathrm{d}A_{MPV}}{\mathrm{d}U_{bd}} = \frac{-\mathrm{d}U_{bd}}{dT} \frac{1}{V - U_{bd}} \tag{7.7}$$

As it has been already mentioned in the beginning of the section 7.1 the dependence of U_{bd} on the temperature for MPPCs in [14] shows a linear trend: $\mathrm{d}U_{bd}/\mathrm{d}T = 56 \pm 0.1$ mV/K. If the difference $V - U_{bd}$ is high enough, we can assume K_T to be constant. The value of K_V can be also assumed to be constant because of the range of applied voltage (Figure 7.2).

The advantage of estimation of K_T and K_V is that we can find the temperature and voltage slopes for all cells only from the knowledge of K_T and K_V.

Distributions of K_T and K_V for CERN 2007 and FNAL 2008 runs are shown in Figures 7.7, 7.8 and 7.9. Distributions of K_T or K_V are not symmetrical and

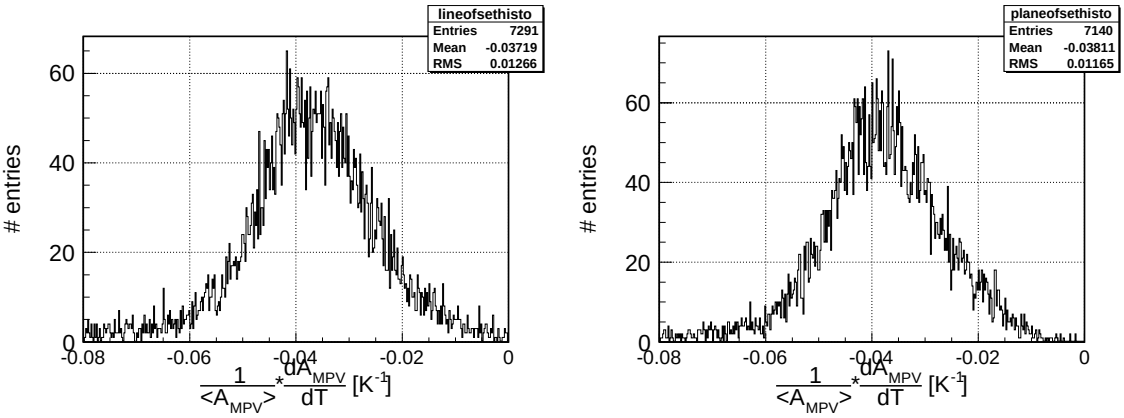

Figure 7.7: Distribution of K_T for the CERN 2007 runs obtained by the line fit (left) and planar fit (right).

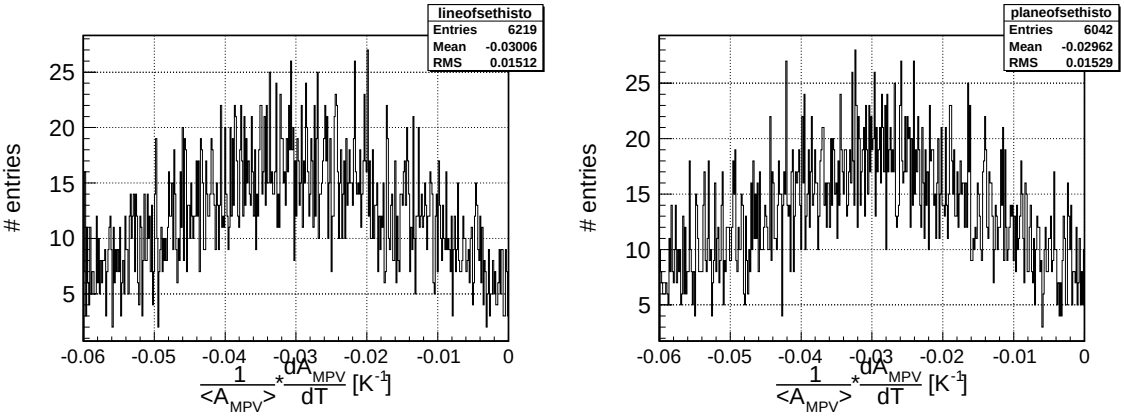

Figure 7.8: Distribution of K_T for the FNAL 2008 runs obtained by the line fit (left) and planar fit (right).

they have tails at bigger values of $|K|$. Such a behaviour is understandable when we check one characteristic temperature or voltage slope. It was found that some

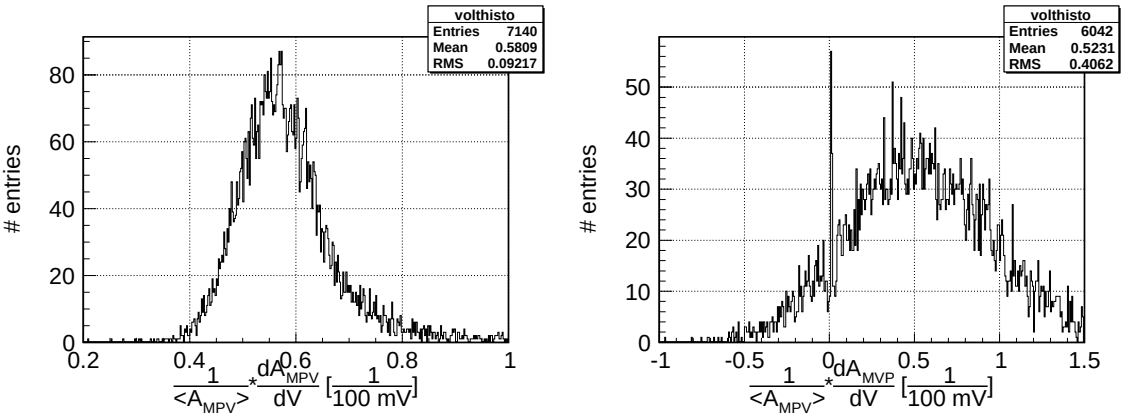

Figure 7.9: Distribution of K_V for the CERN 2007 (left) and FNAL 2008 (right) runs obtained by the planar fit method.

of cells have jump in value of A_{MPV} for higher temperatures. It is illustrated for one cell in Figure 7.10.

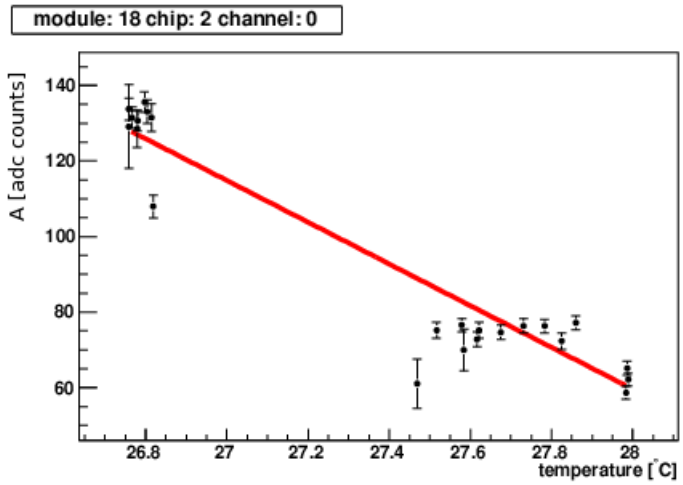

Figure 7.10: The temperature dependence of A_{MPV} for one selected cell with unexpected behaviour.

Since there have been previously determined the mean of the K_T and K_V, we can make an comparison of obtained results. The comparison of K_T and K_V for various methods is shown in Table 7.1.

There is visible different mean value of K_T for CERN 2007 and FNAL 2008 runs. Such a difference can be explained by different nominal value of beam energies.

method, run period	$100 \cdot \langle K_T \rangle$ [$\% \cdot \mathrm{K}^{-1}$]	$100 \cdot \mathrm{RMS}_{K_T}$ [$\% \cdot \mathrm{K}^{-1}$]	# entries($K_T > -0.08$)
line, CERN2007	-3.7	1.7	6473
line, FNAL2008	-3.0	-	6024
planar, CERN 2007	-3.8	1.1	6219
planar, FNAL 2008	-3.0	-	6042
line merged	-3.6	1.6	6378
planar merged	-3.7	1.1	7031
previous, CERN 2007	-3.7	1.1	-

Table 7.1: Results for K_T, defined by (7.5), comparison with previous results

method, run period	$100 \cdot \langle K_V \rangle$ [%/100mV]	$100 \cdot \mathrm{RMS}_{K_V}$ [%/100mV]
planar, CERN 2007	5.8	0.9
planar, FNAL 2008	5.2	4.1
previous, CERN 2007	5.6	0.8

Table 7.2: Results for K_V, defined by (7.5), comparison with previous results

7.2.3 Summary of results

We have tried to find the best method for the temperature and voltage corrections estimations. The constrain on the minimum value -8 % and on the maximum value 0 % of temperature slopes has been applied . The cut on the minimun value of slope is given because of the unexpected jump of A_{MPV} for higher temperatures (Fig. 7.10). The method with the maximum number of fitted cells was the plane fit method with common fit of CERN 2007 and FNAL 2008 data sets. On the other side, this method has the worst relative uncertainty of fit. The reason is the discrepancy between the slopes for CERN 2007 and FNAL 2008 data sets for some cells. The method with the smallest uncertainty of the slope is the planar method. The mean relative uncertainty for the CERN 2007 runs, shown in Figure 7.5 is more than 4 times smaller for the planar method. The improvement of fit in term of relative uncertainty of slope is visible also for the FNAL 2008 runs (Fig. 7.6).

The problem of fitting temperature and voltage slopes for individual cells leads to find the mean of K_T and K_V, which is the characteristic quantity of SiPMs as it is shown at the beginning of this section. The spread of K_T and K_V is visible worse for the FNAL 2008 runs (Fig. 7.7 - 7.9) . It correspond to the worse relative uncertainty of slopes for the FNAL 2008 runs in comparison with CERN 2007 runs.

The results of K_T and K_V for all of used methods are in Tables 7.1 and 7.2. The results for all modified methods correspond to the results of previous (default) methods within the error.

Chapter 8

Track finding

The reconstruction of muon track in the HCAL requires a dedicated algorithm to identify the calorimeter cells hit by a muon. In the absence of a magnetic field the muon trajectory lives straight tracks into the calorimeter and a relatively simple algorithm can be used to find the tower of cells penetrated by each particle. On the other hand muons trajectories can be slightly tilted with respect to the calorimeter geometry and cross the boundary between two towers at some depth in the calorimeter itself. In addition, the reconstruction of muons traversing very close to the tile edge can be affected by mis-alignment of calorimeter layers, dead areas between calorimeter cells or shared energy deposition between tiles. These effects slightly complicate the algorithm of track finding if one wants to avoid to inefficiencies which lead to a distortion of the muon energy spectrum, as discussed for Figure 6.5. In the following it will be described how the default track finder has been improved in order to minimize this type of inefficiency. Results presented below were obtained by analyzing of the calibration run 330254 from the testbeam period CERN 2007.

Before applying the track finding algorithm it has to be estimated the rough position of the most probable value of deposited energy by muons MIP_{rough} per every cell. To reduce the pedestal influence, it has to be applied a cut on the minimal value of deposited energy. Then for the track finding we used only hits with the deposited energy above $0.5 \cdot MIP_{rough}$. The information about MIP_{rough} for every cell is used as an input of the trackfinder's Marlin processor. The distribution of muon deposited energy A for a selected cell is shown in Figure 8.1. The energy deposition of hits without an application of track finding is shown with a blue line and with an application of track finding is shown with a black line. The problem of an influence of pedestal events is visible on the right side. In the following steps we used for the term hit only the hits above the $0.5 \cdot MIP_{rough}$ cut.

The default track finding algorithm is simple but sufficiently effective algorithm to find muon tracks. First step is to build from any hit called "seed hit" a

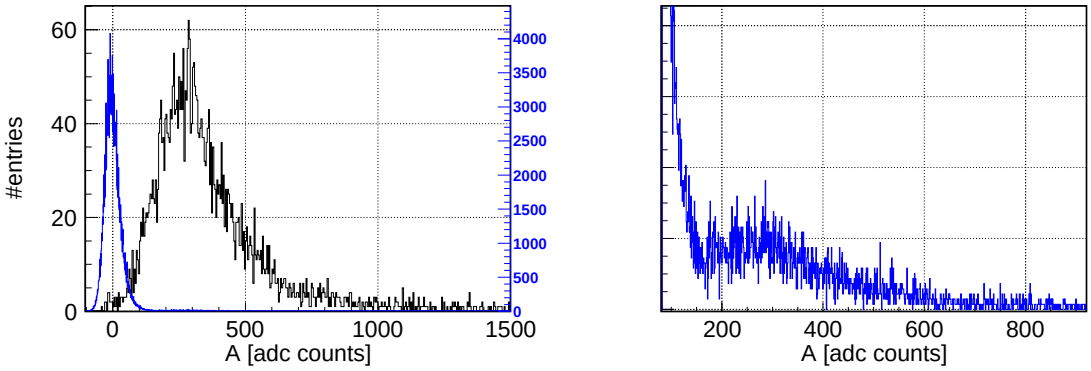

Figure 8.1: Left: The comparison between the distribution of deposited energy of all hits in a tile (blue line) and of the hits selected as muon hits after applying the muon track finder. Right: The detail of the distribution of deposited energy of hits without track finding algorithm.

tower with the width of the corresponding cell size through all layers. This tower is perpendicular to the layers. The "seed hit" has to be from the fine modules. If the number of hits in tower is above defined fixed number we have found the track. All of cells, which are in the tower are also assumed to be the track hits.

The disadvantage of such a procedure is, that it is only possible to find perpendicular tracks to layers. It can happen that a bulk of hits are in the neighbour cells due to non perpendicular track, but the number of hits in tower is above a threshold. Then there are filled in tower also pedestal hits. The second disadvantage is the constrain on the angle of tracks.

We have tried to solve both of disadvantages with the modification of the track finding algorithm. The used algorithm is commonly called the *follow your nose (FYN)* algorithm. The algorithm correspond to the name. We start from the first layer with the hit and continue in the subsequent layers searching for the hits in the nearest cells. The algorithm is also modified for the assumption of the small angles.

8.0.4 The algorithm of track finding

The algorithm of the default method

An assumption for the default method is that the muon track is strictly perpendicular to the layers or more precisely, that all of hits of one track are projected to the same point. So the algorithm of the default track finding can be described in the following steps:

1. Take the first hit from all of the recorded hits of one muon event. We call this hit "seed hit".

2. All hits, with x,y coordinates corresponding to the coordinates of the "seed hit" within plus-minus half of the cell size are considered as track hits.

3. If the track have less than N_T hits, where N_T is a fixed parameter, the track is excluded from assumption.

4. Subsequently also hits with deposited energy below $0.5 \cdot MIP_{rough}$ having x,y coordinates as the seed hit, are assumed as the track hits.

5. Check, if there are also another muon tracks in the same event.

The algorithm of the modified track finding method
We have generalized the track finding algorithm to take in account also muon tracks with not perpendicular tracks to the layers.
All hits are ordered by the layer number.

1. Take the "seed hit" from recorded hits. The "seed hit" is now any recorded hit with the smallest layer number.

2. Check for the second hit. The second hit is searched in the nearest subsequent layer in cells with the same coordinates within plus-minus the cell size.

3. From x,y coordinates of the "seed hit" and the last already found hit, we compute the extrapolated position of the hit in a nearest subsequent layer. If the extrapolated coordinates correspond to the next hit within the cell size, the next hit is taken as a track hit. This step is repeated until the last layer is reached.

4. The "seed hit" and the last hit define the track. We take also in account the hits with coordinates corresponding to the track coordinates within the half of the cell size.
   This procedure is used only if the following procedure is not successful: If there is no hit in a layer, check for the first layer with the layer number higher and lower, where it can be found any track hit. If the coordinates of track hits with lower and higher layer numbers are the same, fill the layer without hit with the hit of x,y coordinates as coordinates of already found track hits. Such a procedure is efficient only for small angles of tracks.

5. Check, if there are also another muon tracks in the same event.

8.1 Efficiency of the track finding

This section is devoted to the study of the efficiency of the $0.5 \cdot MIP_{rough}$ cut.
From extrapolated final fit function defined by (6.5) we can compute so-called

MIP detection inefficiency, which is equal to $\int_0^{cut} \mathrm{d}\epsilon(l \otimes g)(\epsilon) / \int_0^K \mathrm{d}\epsilon(l \otimes g)(\epsilon)$, where $K \gg 1$ and *cut* is in our case equal $0.5 \cdot MIP_{rough}$. The distribution of MIP detection inefficiencies for every cell is shown in Figure 8.2. An inefficiency

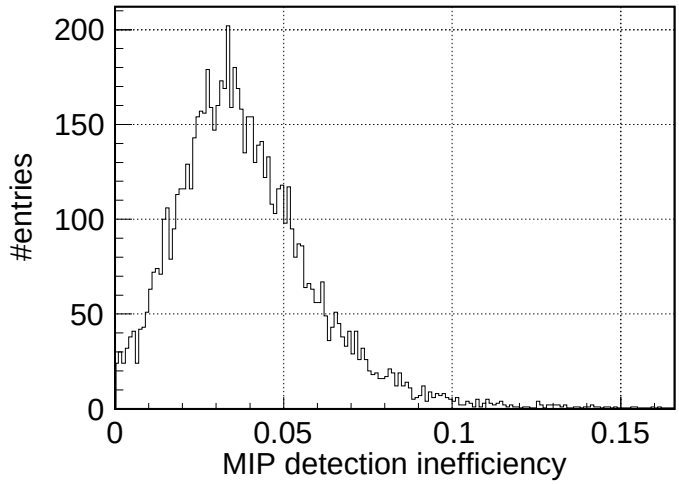

Figure 8.2: MIP detection inefficiency $\int_0^{0.5 \cdot MIP_{rough}} \mathrm{d}\epsilon(l \otimes g)(\epsilon) / \int_0^{K \gg 1} \mathrm{d}\epsilon(l \otimes g)(\epsilon)$.

of finding track can be evaluated as a probability to have the number of hits of a track smaller than a threshold for the minimal number of hits per track. If the maximal number of entries per track is N, threshold for the minimal number of hits per track N_T, MIP detection inefficiency I same for all cells, then the probability to have number of hits per track less than selected minimal number of hits per track S can be computed as

$$S = \sum_{i=0}^{N_T - 1} \binom{N}{i} I^{N-i} (1 - I)^i. \tag{8.1}$$

From Figure 8.2 we can determine the mean of the MIP detection inefficiency $I = 0.035$. The assumption of the same inefficiency for all cells is not precise but sufficient for rough estimation of the quantity S. Then for $N = 38$ and $N_T = 16$ we have $S \approx 10^{-24}$, which is really low. The inefficiency $S = 1\%$ is reached only with the minimal number of hits per track $N_T = 34$. The number $N_T = 16$ was used in the default track finding algorithm. The conclusion is, that the threshold for the minimal number of hits per track equal to $N_T = 16$ is sufficiently low. Also we can see, that the number of hits per track should be sufficiently high to find the track.

We have also analyzed the distribution of the number of hits per track. For this purpose we have calculated two different quantities.

The first quantity, called *efficiency1* is defined as the ratio of the number of hits per track and the number of used layers.
The second quantity, called *efficiency2* is defined as the ratio of the number of hits per track and the number of layers between the first and the last hit layer. The distribution of *efficiency1* and *efficiency2* is shown in Figure 8.1.

There is a significant difference between the distribution of *efficiency1* and

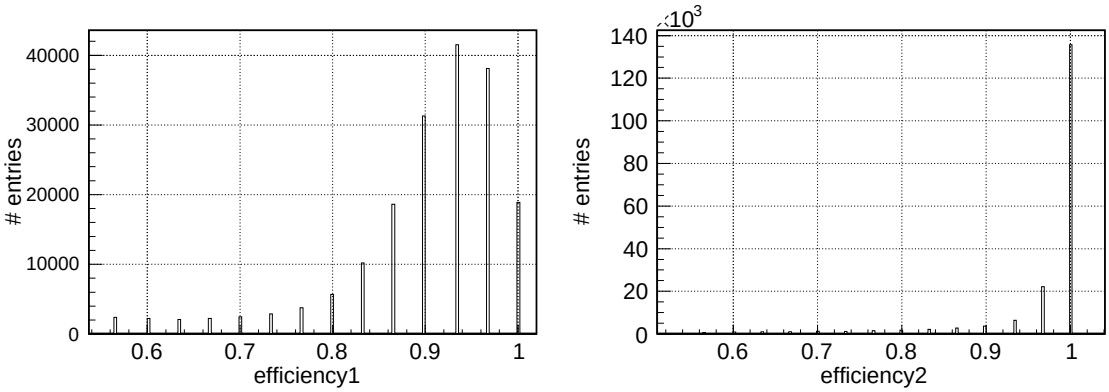

Figure 8.3: The distribution of a ratio of number of found hits per track and number of used layers for track finding called *efficiency1* (left). The distribution of a ratio of number of found hits per track and number of layers between the first and the last hit of track called *efficiency2* (right).

efficiency2. The distribution of *efficiency1* has surprisingly high contribution for low values of *efficiency1* with respect to the expectation that muons penetrate all layers. It means, that some tracks end before reaching the last layer. The problem can be also caused by improper adjustment of $0.5 \cdot MIP$ cut.

8.2 Comparison of modified and default track finding

The reason for the modification of the track finding algorithm for calibration process was a contribution of pedestal events which influence the adjustment of the range of fit of cell response. The distribution of the energy deposition for all cells for the modified and the default track finding method is shown in Figure 8.4. It is clear that the modified track finding algorithm can suppress the contribution of pedestal.

As it was previously mentioned, the modified track finding is made without any constrain on the track angles. The track angle θ is defined as an angle between the beam line direction and the direction of the track. The distribution of tangent of the track angle θ is shown in Figure 8.5. The distribution of number

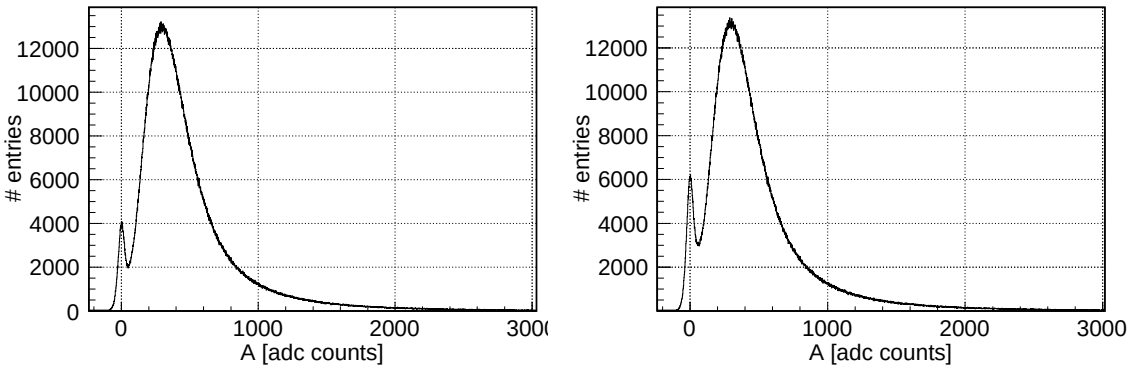

Figure 8.4: Comparison of muon energy deposition A in in all cells for the modified (left) and default (right) track finding algorithm.

of transversed muon tracks per cells for the first *fine* layer (left) and the last *course* layer (right) is shown in Figure 8.6.

We can see, that there are also muon tracks with an angle θ not equal to the zero in the calibration run where the beam line was perpendicular to the layers. From the distribution of number of muon tracks per cell we can see the sufficiently homogenous distribution of the beam profile. There is also the difference $\sim 10^3$ in the number of tracks in the first and the last layer. It is visible from the distribution of $\tan\theta$, that the reason for the difference could be non perpendicular muon tracks.

The distribution of number of tracks per cell for both track finding algorithms is shown in Figure 8.7. A horizontal lines in the correlation plot are understandable. The reason for them is the algorithm of the default method, where we have the same number of tracks in all cells, which are on the line perpendicular to layer.

The correlation between the most probable values A_{MPV} of fit function 6.5 for data obtained from the distribution of the deposited energy of muons per cell for the modified and default track finding algorithm is shown in Figure 8.8 on the left side. The distribution of the shift defined as

$$shift = 2 * \frac{A_{MPV(modified)} - A_{MPV(default)}}{A_{MPV(modified)} + A_{MPV(default)}}, \tag{8.2}$$

is shown on the right side. $A_{MPV(modified,(default))}$ is the most probable value of fit for the modified (default) track finding algorithm. We can see that both methods are sufficiently correlated without a bias of the most probable value.

The difference between both methods is visible in the distribution of the relative uncertainties σ_{MPV}/A_{MPV}, where σ_{MPV} is the error of A_{MPV} from fit. The distributions of σ_{MPV}/A_{MPV} for both methods are shown in Figure 8.9.

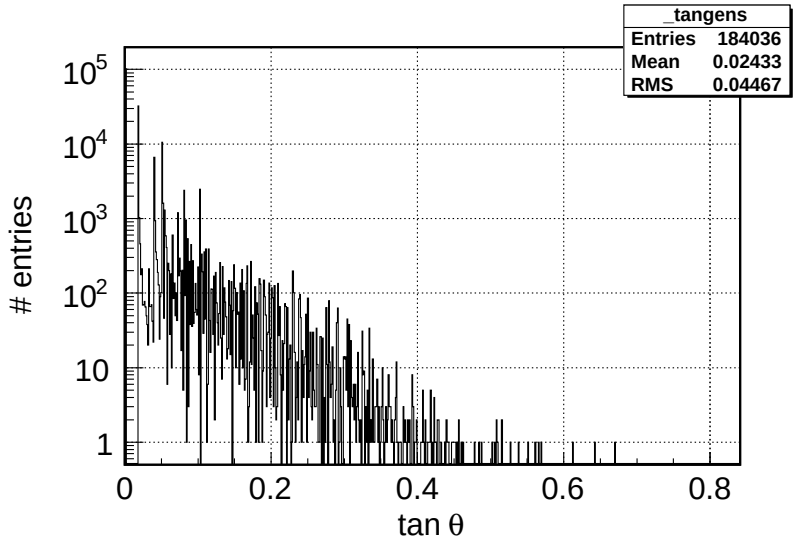

Figure 8.5: Distribution of tangent of angle θ between the beam line direction and the direction of the track.

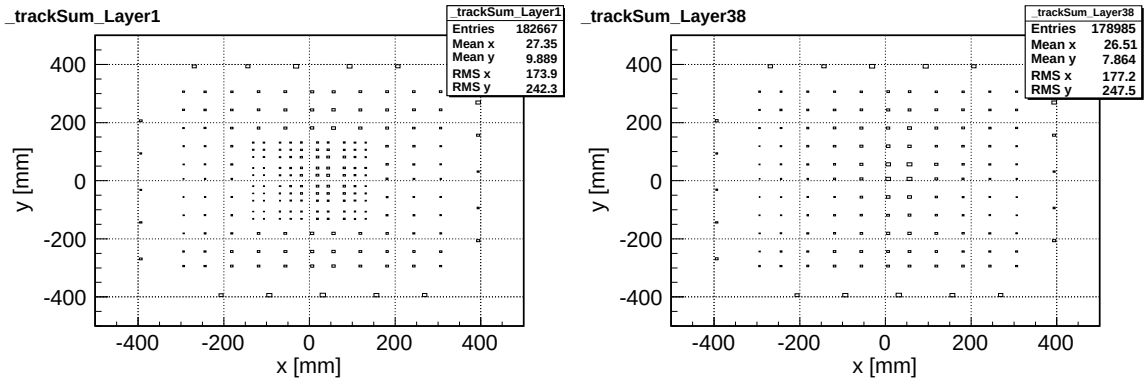

Figure 8.6: The distribution of number of transversed muon tracks per cells for the first *fine* layer (left) and the last *course* layer (right).

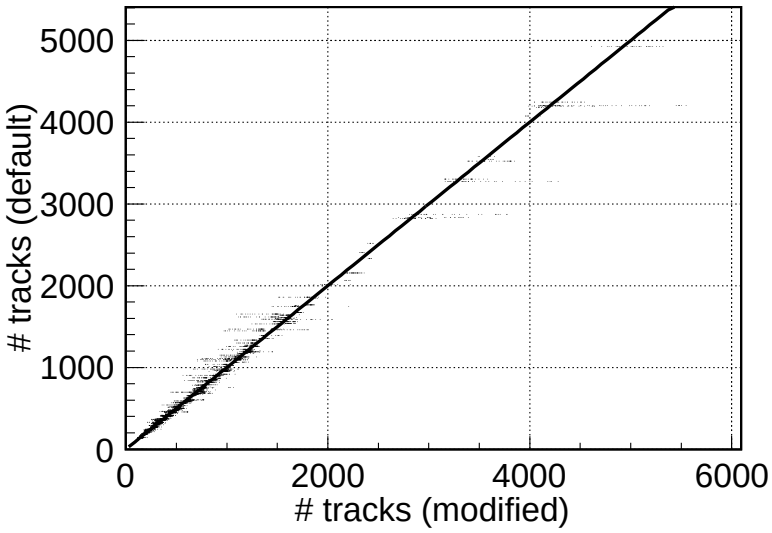

Figure 8.7: The distribution of the number of tracks per cell for both track finding algoritms.

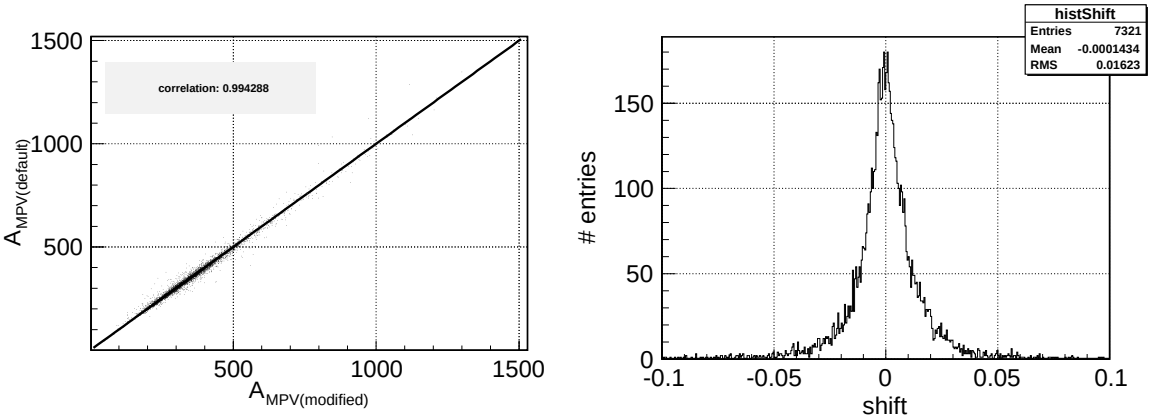

Figure 8.8: The correlation between the most probable values per cell obtained by the default and the modified track finding algorithm (left). The distribution of the shift defined by (8.2) for every cell (right).

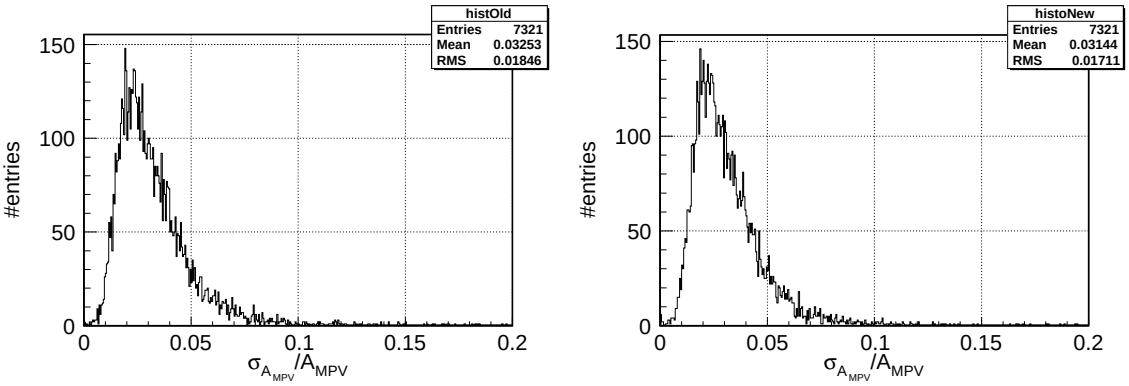

Figure 8.9: The distribution of relative uncertainty of MPV σ_{MPV}/MPV obtained from fit for the default track finding (left) and modified track finding (right) algorithm.

The modified track finding algorithm provides slightly more stable determination of a MPV from fit function.

8.3 Angular dependence of muons in pion runs

The pion runs are the most important runs for the verification of the AHCAL performance. As it is known, the charged pions decay mainly to muons in the process $\pi^{\pm} \rightarrow \mu^{\pm} + \nu_{\mu}$. Therefore we can find in the pion runs also muons. We are able to select the muon tracks from the pion runs with an additional constrains.

Selection of muons from pion runs was made with the help of additional informations from ECAL and TCMT. To select only muons from the AHCAL, we have done several cuts on energy and number of hits in ECAL and TCMT.
The cut on the minimal number of hits per a muon event have the same meaning as for the muon beams. It is done to be sure, that we have sufficient number of hits per track.
The cut on the maximal number of hits per a muon event is obvious. We want to exclude pions which are showering mainly in the AHCAL.
The cut on maximum deposited energy is done as an additional cut for the exclusion of pions.
All runs, which we have used are from the CERN 2007 testbeam period. The angle of the run is defined as an angle between the beam direction and the direction of line perpendicular to the layers. We have used only pion runs at 0, 10, 20 and 30 degrees with sufficient contamination of muons. . The temperature and voltage corrections with default values for slopes are also included. The energy of pion beams were in the range from 6 GeV to 180 GeV.

The rotation angle is defined as angle between the beam line and a direction perpendicular to layers. We expect that the length of track in active layer x_α, where α is angle defined above, fulfil the relation

$$x_\alpha = \frac{x_0}{\cos(\alpha)}. \tag{8.3}$$

We can also expect for the deposited energy of muons in angle α

$$E_\alpha = \frac{E_0}{\cos(\alpha)}. \tag{8.4}$$

The dependence of deposited energy of muons in the pion runs on angle α is shown in Figure 8.10. The deposited energy has been obtained as a MPV of the energy distribution. The depicted plot shows that the new track finding is also applicable on the muon events with arbitrary angles.

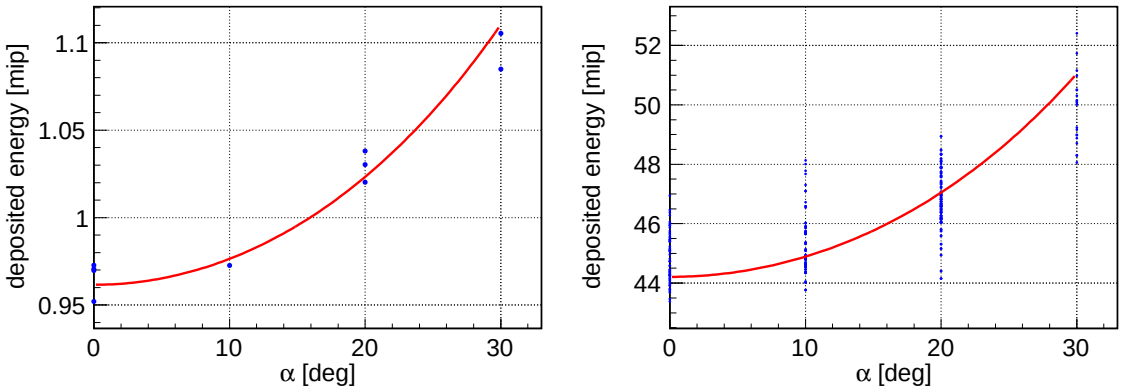

Figure 8.10: Angular dependence of deposited energy of muons in pion runs for the energy of beam 60 GeV and layer 3 (left) and for all of energies of pions, where the deposited energy of muons have been calculated as a sum of energies from all of HCAL layers for every event (right).

8.3.1 Summary of results

We have modified the default track finding algorithm. The main reason for the modification was the distortion of the energy distribution of muons per cell by the pedestal events distribution. The subtraction of excess on zero is visible from Figure 8.4.

The possibility of finding the tracks without any constrain on angle of track has been developed. The angular distribution of events for the calibration run is shown in Figure 8.5.

The relative uncertainty of A_{MPV} has been slightly diminished (Fig. 8.9).

The possibility of using the modified track finding algorithm also for beams, where the beam direction is not perpendicular to the layers, is described in section 8.3. The muons selected from the pion runs in different angles of beam direction have been used. The angular dependence of deposited energy of muons is shown in Figure 8.10.

Chapter 9

Summary

In this thesis we have present results of our calibration methods for the AHCAL, which includes the fit of the distribution of the muon deposited energy, dependence of the cell response on the temperature and voltage and the track finding algorithm.

For the purpose of finding the most probable value (MPV) of energy deposited by muons, we have developed a program for fitting the distribution of deposited energy for all cells of the AHCAL. The two modifications have been applied. The likelihood fitting method instead the χ^2 fitting method and the use of the Fast Fourier Transformation for evaluation of the convolution fitting function. It allowed us to use also the cells with very low statistics. When comparing both methods, we have found a bias of MPVs. We have tried to find, which method is biased to the real MPV. From comparison of MPVs determined by smoothing histograms, we have found possible bias of the χ^2 method and no bias of the likelihood method.

For the purpose of finding the temperature and voltage dependence of MPV, we have also modified the default method. We have estimated the temperature dependence of the SiPMs by including the voltage settings different to the nominal voltage settings. We could than make a planar fit instead of the line fit and also simultaneously estimate the voltage dependence of the SiPMs. The results for the temperature and voltage characteristics of the SiPMs agree with the previous results.

The track finding algorithm was modified with the possibility to find muons, which are not perpendicular to the calorimeter layers. It allowed us to use the modified track finding processor for the selection of muons in pion runs where the beam line is not perpendicular to the layers. The $1/\cos$ dependence was observed. We have also studied the efficiency of the track finding. The mean ratio between the number of found hits and the number of layers is about 0.90 and the ratio between the number of found hits and the number of layers between the first and the last hit is close to the 1.

The obtained calibration constants with the corrections on the temperature and voltage are stored in the database of the FLC working group and are available for further analyses.

Bibliography

[1] *ILC Reference Design Report*, arXiv: 0712.1950v1, 2007.

[2] *The International Large Detector, Letter if Intent*, ILD Concept Group, 2009 (unpublished).

[3] *ILC reference design report volume 4 - detectors*, arXiv: 0712.2356v1, 2007

[4] J. Brau, Y. Okada and N. Walker *ILC Reference Design Report Volume 1 - Executive Summary* 2007.

[5] The CALICE Collaboration *Construction and Commissioning of the CALICE Analog Hadron Calorimeter Prototype*, unpublished.

[6] Mark Thomson *Progress with Particle Flow Calorimetry*, arXiv:0709.1360v1 [physics.ins-det].

[7] Mark Thomson *Calorimetry and Particle Flow at the International Linear Collider*, RAL HEP Forum, 2006.

[8] I.G. Knowles, and G.D. Lafferty, J. Phys. **G23** 1997 731.

[9] M.G. Green, S.L. Lloyd, P.N. Ratoff and D.R.Ward *Electron-Positron Physics at the Z*, IoP Publishing 1998.

[10] B. Dolgoshein *el al Status report on silicon photomultiplier development and its application*, Nucl. Instr. and Methods in Physics Research A 563 368-376, 2006

[11] P. Buzhan *el al An Advanced Study of Silicon Photomultiplier*, ICFA Instrumentation Bulletin 23, 2001.

[12] E. Garutti, M. Groll, A. Karakash, and S. Reiche *Magnetic field dependence studies for silicon photomultiplier* LC-DET-2004-025.

[13] The CALICE Collaboration *Electron data with the CALICE tile HCAL prototype at the CERN test-beam* CALICE Analysis Note 010, 2008.

[14] S. Uozumi *Study and Development of the Multi-Pixel Photon Counter for GLD Calorimeter Readout*, PoS PD07, 2007.

[15] L. Weuste *A Study of Track Segments within Hadronic Showers with Highly Granular Hadronic Calorimeter* , Master's thesis, Ludwig-Maximilians-Universität, 2009.

[16] B. Lutz *Commisioning of the Readout Electronics for the Prototypes of a Hadronic Calorimeter and a Tailcatcher and Muon Tracker*, Master's thesis, Universität Hamburg, 2006.

[17] N.Feege *Silicon Photomultipliers: Properties and Application in a Highly Granular Calorimeter*, Master's thesis, Universität Hamburg, 2008.

[18] M. Groll *Construction and Commissioning of a Hadronic Test-Beam Calorimeter to Validate the Particle-Flow Concept at the ILC*, DESY-THESIS-2007-018, 2007.

[19] C. Leroy, P.G. Rancoita *Principles of radiation interaction in matter and detection*, World Scientific Publishing Co. Pte. Ltd., 2004

[20] E. Garutti, A. Vargas and the others of the CALICE group *private communication*